Research Square

Preprints are preliminary reports that have not undergone peer review.
They should not be considered conclusive, used to inform clinical practice,
or referenced by the media as validated information.

A Long-Term Tropical Cyclone RMW Dataset in the Western North Pacific Based on a Bayesian Consensus of Multiple Estimates

Udai Shimada

ushimada@mri-jma.go.jp

Meteorological Research Institute

Taiga Tsukada

Colorado State UniversityCooperative Institute for Research in the Atmosphere

Article

Keywords: Tropical Cyclones, Radius of maximum wind, Long-term dataset, Satellite observation

Posted Date: June 10th, 2026

DOI: https://doi.org/10.21203/rs.3.rs-9904577/v1

License: This work is licensed under a Creative Commons Attribution 4.0 International License.
Read Full License

Additional Declarations: No competing interests reported.

A Long-Term Tropical Cyclone RMW Dataset in the Western North Pacific Based on a Bayesian Consensus of Multiple Estimates

Udai Shimada[1,2]

ORCID id: 0000-0002-6971-2693

Correspondence: ushimada@mri-jma.go.jp

Taiga Tsukada[3]

ORCID id: 0000-0003-2036-308X

Author details

1 Meteorological Research Institute, Japan Meteorological Agency, Japan

2 Typhoon Science and Technology Research Center, Yokohama National University, Japan

3 Cooperative Institute for Research in the Atmosphere, Colorado State University, Fort Collins, Colorado

Abstract

The radius of maximum wind (RMW) is one of the key parameters for characterizing the

structure of tropical cyclones (TCs). Although multiple methods have been developed to estimate the RMW, their estimates can sometimes differ substantially and are not always available, making it difficult to construct a comprehensive long-term RMW dataset. This study develops a Bayesian consensus method to derive a single RMW estimate from multiple RMW estimates. In this framework, the posterior probability distribution of the RMW is estimated using likelihoods constructed from method-specific error distributions combined with an outlier distribution, and the final RMW is determined as the maximum a posteriori (MAP) estimate. By explicitly accounting for an outlier distribution for each estimation method, the proposed method can determine a reasonable RMW close to one of the clusters even when the estimates split into two clusters. Using this consensus method and, as a primary source, estimates from satellite-based global precipitation data and from infrared and microwave satellite data for TCs with an eye, a long-term RMW dataset is constructed at 3-h intervals for 631 TCs in the western North Pacific during 2000–2025. Verification of the consensus RMW estimates shows that errors decrease with increasing TC intensity and posterior probability, and that posterior probability itself serves as an indicator of estimate reliability. This new RMW dataset enables a realistic representation of the inner-core structure, particularly small RMWs, which were difficult to estimate before the advent of synthetic aperture radar (SAR)-derived winds and in the

absence of aircraft observations.

Keywords

Tropical Cyclones, Radius of maximum wind, Long-term dataset, Satellite observation

Statements and Declarations

Funding

JSPS KAKENHI Grant 23K13172 and JST Moonshot JPMJMS2282.

NOAA Cooperative Agreement NA24OARX432C0007.

Competing interests

The authors declare that they have no competing interests.

Author Contributions

Both authors contributed to the conception and design of the study. U.S. performed data collection and analysis, wrote the main text of the manuscript, and prepared the figures and the table. T.T. wrote some parts of the manuscript and prepared a few figures. All authors reviewed the manuscript.

Data Availability

GSMaP data are available at https://sharaku.eorc.jaxa.jp/GSMaP/index.htm. ERA5 data are available from the Copernicus Climate Change Service (C3S) Climate Data Store (CDS) (Hersbach et al. 2023). The Tropical Cyclone Precipitation, Infrared, Microwave, and Environmental Dataset (TC PRIMED) is available from the NOAA NCEI (Razin et al. 2023a). Information on the availability of successive geostationary IR satellite data is provided at https://www.data.jma.go.jp/mscweb/en/product/library_data.html. SAR wind data are available from the website of STAR (2026). ASCAT wind data are available from NASA (2026). JMA and JTWC best track data are obtained from the IBTrACS Version 4r01 dataset available at https://www.ncei.noaa.gov/products/international-best-track-archive. The RMW dataset constructed in this study is available at https://doi.org/10.5281/zenodo.20406310.

1 Introduction

The radius of maximum wind (RMW) is a key parameter for characterizing the wind structure of tropical cyclones (TCs), together with the maximum wind speed (V_{max}) and outer size, as these parameters are physically related (Emanuel and Rotunno 2011; Chavas and Lin 2016). The magnitude of the RMW is associated with subsequent changes in TC intensity (Carrasco et al. 2014). TC rapid intensification often occurs after rapid RMW contraction (e.g., Stern et al. 2015; Wu and Ruan 2021; Li et al. 2022). The RMW can rapidly jump from the inner eyewall to the outer eyewall during an eyewall replacement cycle (e.g., Willoughby et al. 1982; Black and Willoughby 1992; Sitkowski et al. 2011). RMW information is used for wind structure construction (e.g., Chen et al. 2025; Liu et al. 2025; Tao et al. 2026), which is also utilized for forecasting ocean waves and storm surge (e.g., Aijaz et al. 2019). While recently developed artificial intelligence (AI)-based weather models have demonstrated significant improvements in TC track forecasts, they have shown negative biases and poor representation of TC intensity and structure (e.g., Yamaguchi et al. 2025; DeMaria et al. 2025). Such weaknesses can be mitigated if a reliable RMW dataset for improved model training is available. Given the importance of the RMW, a WMO workshop has called for the development of methods to construct more accurate RMW datasets (e.g., Rogers et al. 2023; Ito et al. 2025).

Recently, new RMW estimation methods have been developed, and multiple RMW estimates have become available at the same analysis time. One reason for this progress is the availability of accurate RMWs from spaceborne synthetic aperture radar (SAR) observations, which provide detailed TC wind fields with a high spatial resolution (~500 m to 3 km), although the observation frequency with full TC coverage is still low (Mouche et al. 2017, 2019, 2026; Combot et al. 2020; Vinour et al. 2021; Shimada et al. 2024; Tsukada et al. 2025; Avenas et al. 2026). Methods developed using SAR-derived RMWs as ground truth include those based on outer wind radii and eye size derived from infrared and passive microwave satellite observations (Avenas et al. 2023; Tsukada and Horinouchi 2023; Shimada 2025). In addition to these new approaches, previously developed methods (Willoughby and Rahn 2004; Mueller et al. 2006; Kossin et al. 2007; Vickery and Wadhera 2008; Lajoie and Walsh 2008; Knaff et al. 2015; Chavas and Knaff 2022), as well as recent machine-learning-based methods (e.g., Zhuo and Tan 2021, 2023; Lu et al. 2022), are also applicable for estimating the RMW. However, RMW estimates can differ substantially among methods, their time series may fluctuate irregularly, and some methods do not always provide estimates due to limited data availability.

Although many RMW estimation methods have been developed, to our knowledge, a long-term RMW dataset extending back several decades, with homogeneous quality

106 throughout the entire period, has not yet been constructed. To achieve this, a consensus
107 method is required to derive a single representative RMW from multiple RMW estimates.
108 Such a consensus RMW cannot be obtained by a simple arithmetic average of the
109 estimates. For example, an arithmetic average is inappropriate in cases of TCs with
110 concentric eyewalls, where one method estimates the RMW near the inner eyewall while
111 another estimates it near the outer eyewall. Additionally, ideal RMW estimates intended
112 for diverse applications should (i) evolve smoothly over time to represent the scale of the
113 TC inner core, (ii) capture variations associated with eyewall replacement cycles, (iii) be
114 continuously available throughout the TC life cycle, and (iv) maintain homogeneous data
115 quality across the entire period.

116 The purpose of this study is to develop a consensus method of RMW estimation based
117 on a Bayesian framework and to construct a long-term RMW dataset. Specifically, the
118 posterior probability distribution of the RMW is estimated using likelihoods constructed
119 from method-specific error distributions combined with an outlier distribution, and the
120 final RMW is determined as the maximum a posteriori (MAP) estimate. By explicitly
121 accounting for an outlier distribution for each method, the posterior distribution can
122 exhibit multimodality. This approach can determine a reasonable RMW close to one of
123 the clusters even when the estimates split into two distinct clusters, rather than yielding

an intermediate value between them.

For the construction of the long-term RMW dataset, this study targets 631 TCs that occurred in the western North Pacific from 2000 to 2025, with a temporal resolution of 3 h. To ensure homogeneous quality throughout the period, RMWs are estimated using only observations that have been continuously available since 2000. Additionally, new estimation methods are developed using global satellite-derived precipitation data (Global Satellite Mapping of Precipitation, GSMaP; Kubota et al. 2007, 2009) and atmospheric reanalysis data [the European Centre for Medium-Range Weather Forecasts (ECMWF) fifth-generation reanalysis product, ERA5; Hersbach et al. 2020] to provide RMW estimates at all analysis times and to suppress irregular temporal fluctuations. The proposed consensus method selectively determines an RMW value closest to the most accurate estimate among the available methods.

In this study, the RMW is defined as the radius of maximum azimuthally averaged wind, rather than the radius of the local maximum wind speed (hereafter, the local RMW), following previous studies (e.g., Vinour et al. 2021; Avenas et al. 2023; Tsukada and Horinouchi 2023; Shimada 2025). This definition allows the RMW to represent the horizontal scale of the inner-core region of large positive vorticity in the Northern Hemisphere, as the positive vorticity in a modified Rankine vortex decreases rapidly

142 outside the RMW. Additionally, this definition reduces sensitivity to local maxima caused
143 by instantaneous gusty wind speeds and is therefore expected to yield more stable RMWs
144 when satellite observations are used as ground truth. One caveat is that a relatively large
145 difference may exist between the local RMW and the RMW defined in this study for TCs
146 with elliptical eyewalls or concentric eyewalls.

147 The rest of the paper is organized as follows. Section 2 describes the data used in this
148 study. Section 3 presents the RMW estimation methods used in the consensus. Section 4
149 describes the consensus method. Section 5 presents the verification results of the
150 consensus, including case studies. Section 6 presents the long-term RMW dataset. Section
151 7 provides a summary of the study.

152

153 2 Data

154 In this study, best track V_{max} data from the Japan Meteorological Agency (JMA) are
155 used, except in Sect. 6. Because JMA V_{max} is not provided during the TD stage, it is
156 extrapolated assuming a linear inverse relationship with the central pressure available
157 during the TD stage. Consequently, the extrapolated V_{max} may occasionally reach TS
158 strength (18 m s^{-1}) during the TD stage. In Sect. 6, V_{max} and RMW data from the Joint
159 Typhoon Warning Center (JTWC; Howell et al. 2025) are used for comparison.

The following datasets are used for RMW estimation: GSMaP data with a spatial resolution of 0.1°, ERA5 10-m wind data with a spatial resolution of 0.25°, intercalibrated passive microwave (PMW) satellite data at 85–91 GHz, and geostationary infrared (IR) satellite observations. Hourly GSMaP data are mapped onto TC-centered polar coordinates and averaged over a 7-h window to mitigate differences in precipitation amounts among satellite sensors, following Shimada et al. (2017). The TC center position at each time is derived from hourly interpolated best track data provided by the JMA. Details of GSMaP data processing and its applicability to TCs are described in Shimada et al. (2017, 2018). The TC center in the ERA5 data is identified as the location of the minimum in the smoothed ERA5 mean sea level pressure field, following Aizawa et al. (2024). The ERA5 10-m wind fields are then interpolated onto TC-centered polar coordinates. The PMW satellite data are obtained from the TC PRIMED dataset (Tropical Cyclone Precipitation, Infrared, Microwave, and Environmental Dataset; Razin et al. 2023b). This dataset includes observations from the Special Sensor Microwave Imager (SSM/I), the Special Sensor Microwave Imager/Sounder (SSMIS), the Tropical Rainfall Measuring Mission (TRMM) Microwave Imager (TMI), the Advanced Microwave Scanning Radiometer for the Earth Observing System (AMSR-E), the Advanced Microwave Scanning Radiometer 2 (AMSR2), and the Global Precipitation Measurement

178 (GPM) Microwave Imager (GMI). Geostationary IR satellite observations are from the
179 JMA (e.g., Bessho et al. 2016). To ensure consistency in horizontal resolution among
180 successive satellites, the IR data are resampled to a spatial resolution of 5 km in this study.
181 This study uses SAR wind data and Advanced Scatterometer (ASCAT) wind data as
182 reference datasets for the development of RMW estimation methods and for the
183 verification of RMW estimates. While the SAR wind data are used for TCs at tropical
184 storm (TS) intensity or higher, the ASCAT data are used for TD cases and TS cases with
185 V_{max} = 18 m s^{-1}. The SAR wind data, including TC center position information, are
186 obtained from the National Oceanic and Atmospheric Administration's (NOAA) Center
187 for Satellite Applications and Research (STAR) Tropical Storm Cyclone Winds page
188 (STAR 2026) for the period 2015–2025, with a horizontal resolution of 3 km. Data from
189 2015 to 2024 are used as the reference dataset (unless otherwise noted), whereas data
190 from 2025 are used for verification. Cases with two or more distinct peaks in the radial
191 profile of the azimuthally averaged SAR wind speed are excluded from the reference
192 dataset to ensure the derivation of a single RMW estimate. The ASCAT wind data are
193 obtained from the National Aeronautics and Space Administration (NASA) Earthdata
194 Search (NASA 2026) for the period 2012–2025, with a horizontal resolution of 25 km.
195 The TC center is defined as the location of the maximum streamfunction derived from

196 the vorticity field computed from ASCAT wind vectors. The ASCAT wind fields are then
197 bilinearly interpolated onto TC-centered polar coordinates with a radial spacing of 2 km
198 to derive the RMW. Due to the coarse spatial resolution and possible center displacement,
199 however, the RMW derived from the azimuthally averaged ASCAT wind is located near
200 the TC center in ~10% of the samples. To avoid this, the radius of the local maximum
201 ASCAT wind (i.e., the local RMW) is adopted as the RMW when the azimuthally
202 averaged RMW is less than 150 km, as the local RMW is generally consistent with it
203 within this range.
204

205 # 3 RMW estimation methods

206 In this study, six estimation methods are incorporated into the consensus framework
207 to construct a long-term RMW dataset, four of which are newly developed. These new
208 methods are needed because RMW estimates are required at all analysis times, including
209 the TD stage, over a long period extending back to 2000 using a homogeneous dataset,
210 requirements that are not fully satisfied by previously developed methods. In this section,
211 two GSMaP-based methods ($RMW_{\mathrm{GSMaP}}^{\mathrm{TS+}}$ and $RMW_{\mathrm{GSMaP}}^{\mathrm{TD}}$; see Appendix A for the
212 notation used in this paper), a modified Rankine vortex method ($RMW_{\mathrm{Rankine}}^{\mathrm{TS+}}$), an ERA5-
213 based method ($RMW_{\mathrm{ERA5}}^{\mathrm{TD}}$), an IR-based method ($RMW_{\mathrm{IR}}$), and a PMW-based method

214 (RMW_{PMW}) are introduced.

215 **3.1 Error distribution**

216 The Bayesian framework necessitates error distributions for each constituent
217 estimates. Consequently, two types of estimation error distributions are adopted in the
218 consensus method in this study: a normal distribution:

219 $$p(\varepsilon) = \frac{1}{\sqrt{2\pi}\sigma} \exp\left[-\frac{(\varepsilon-\mu)^2}{2\sigma^2}\right]$$

220 and a log-normal distribution:

221 $$p(\varepsilon) = \frac{1}{\sqrt{2\pi}\sigma(U-\varepsilon)} \exp\left[-\frac{(\ln(U-\varepsilon)-\mu)^2}{2\sigma^2}\right] \quad (U-\varepsilon > 0)$$

222 where ε denotes the estimation error (defined as the estimate minus the SAR-derived
223 RMW), and μ and σ denote the mean (bias) and standard deviation of the error,
224 respectively. The constant U is an offset introduced for the log-normal distribution and
225 is selected as the value that provides the best fit to the log-normal distribution among
226 multiple candidates near the point at which the frequency rapidly decreases. Specifically,
227 because a log-normal distribution requires $\ln(U-\varepsilon)$ to follow a normal distribution,
228 deviations from linearity in a normal quantile–quantile (Q–Q) plot are evaluated using
229 the root-mean-square error (RMSE), and the value of U that minimizes the RMSE is
230 selected. The error distributions of the RMW estimation methods used in the consensus
231 method are summarized in Table 1.

Table 1: Error distribution parameters of the RMW estimation methods used in the consensus framework.

Estimates	Applicable case	Error distribution	μ [km]	σ [km]	U [km]
$RMW_{\mathrm{GSMaP}}^{\mathrm{TS+}}$	$V_{\max} \geq 18$ m s^{-1}	Normal	1.359	10.617	–
$RMW_{\mathrm{GSMaP}}^{\mathrm{TD}}$	$V_{\max} < 20$ m s^{-1}	Normal	–5.977	81.914	–
$RMW_{\mathrm{Rankine}}^{\mathrm{TS+}}$	$V_{\max} \geq 18$ m s^{-1}	Log-normal	2.981	0.776	14
$RMW_{\mathrm{ERA5}}^{\mathrm{TD}}$	$V_{\max} < 20$ m s^{-1}	Normal	–3.846	67.849	–
RMW_{IR}	Dvorak eye pattern	Log-normal	2.066	0.599	9
RMW_{PMW}	$V_{\max} > 33$ m s^{-1}	Log-normal	2.045	0.518	7

In the following evaluation of the error distribution of RMW estimates from each method, it is necessary to identify and exclude outliers, as outliers can cause the distribution to deviate from a normal or log-normal distribution. For example, in cases of concentric eyewalls, a method may estimate a radius associated with the inner eyewall as the RMW, even though the true RMW is located near the outer eyewall. This results in a large estimation error, which constitutes an outlier far from the true RMW. Additionally, outliers can arise when the precipitation distribution used for RMW estimation is poorly correlated with the actual RMW.

This study employs the median absolute deviation (MAD) as a robust estimator of the standard deviation of RMW estimates in the presence of outliers:

$$\mathrm{MAD} = \mathrm{median}(|\varepsilon_i - \tilde{\varepsilon}|)$$

where ε_i denotes each estimation error and $\tilde{\varepsilon}$ denotes the median of the estimation errors. For a standard normal distribution $\mathcal{N}(0,1)$, the MAD is ~0.6745. Accordingly, assuming that the inlier errors are approximately normally distributed, the MAD computed from the errors can be used to estimate the standard deviation of the underlying inlier distribution as $\hat{\sigma}_{\mathrm{MAD}}$ = MAD/0.6745. For simplicity, assuming that 10% of the data consist of outliers, the central 90% interval of a standard normal distribution is given by ± 1.645. Therefore, $\pm 1.645\hat{\sigma}_{\mathrm{MAD}}$ can be adopted as the criterion for outlier exclusion among errors in this study.

3.2 $RMW^{\mathrm{TS+}}_{\mathrm{GSMaP}}$ and $RMW^{\mathrm{TD}}_{\mathrm{GSMaP}}$

Two GSMaP-based methods are developed to collectively provide RMW estimates at all analysis times, regardless of the presence or absence of a TC eye: $RMW^{\mathrm{TS+}}_{\mathrm{GSMaP}}$ for TS strength and above, and $RMW^{\mathrm{TD}}_{\mathrm{GSMaP}}$ for cases with $V_{\max}$ < 20 m s^{-1} (i.e., including weak TS cases). $RMW^{\mathrm{TS+}}_{\mathrm{GSMaP}}$ exploits a structural relationship in which the radius of maximum precipitation (R_{mp}) is located outside the surface RMW within a sloped eyewall (e.g., Jorgensen 1984). Specifically, R_{mp} is derived from GSMaP data using the following procedures:

i) Apply a 12-h running mean to the 3-hourly azimuthally averaged precipitation to

reduce temporal discontinuities in the precipitation distribution.

ii) Detect R_{mp} as the radius of maximum azimuthally averaged precipitation, and identify the first, second, and third peaks of the azimuthally averaged precipitation in order of increasing radius beyond a radius of 10 km (R_{mp1}, R_{mp2}, and R_{mp3}, when present). Note that R_{mp} is identical to R_{mp1} when $R_{mp} > 10$ km.

iii) When $R_{mp} < 10$ km, set $R_{mp} = R_{mp1}$ if R_{mp1} is available to account for possible TC center displacement.

iv) When $R_{mp} \geq 400$ km, redefine R_{mp} as the candidate with the maximum precipitation among R_{mp1}, R_{mp2}, and R_{mp3}.

v) If R_{mp} differs by 10 km or more from both its values at the previous and subsequent times (± 3 h), and the differences have opposite signs, redefine R_{mp} as the candidate among R_{mp1}, R_{mp2}, and R_{mp3} (in this order) whose difference from the previous value is less than 10 km. If no such candidate exists, replace R_{mp} with the average of the previous and subsequent values.

The regression relating R_{mp} to the SAR-derived RMW is derived using samples with 15 km < R_{mp} < 150 km and maximum azimuthally averaged precipitation rates exceeding 5 mm h^{-1} at each time (Fig. 1a):

$$RMW_{GSMaP}^{TS+} = 0.59\,R_{mp} + 4.68 \quad (1)$$

The correlation is weak for samples with $R_{\mathrm{mp}} < 16$ km, which is attributed to the coarse spatial resolution of GSMaP (0.1°), as small displacements in the TC center position can lead to relatively large errors in cases with small RMWs. Therefore, when $R_{\mathrm{mp}} < 16$ km, set $RMW_{\mathrm{GSMaP}}^{\mathrm{TS+}} = 19$ km, which corresponds to the median value of these samples; otherwise, set $RMW_{\mathrm{GSMaP}}^{\mathrm{TS+}}$ using Eq. (1). Figure 1b shows the estimation error distribution of $RMW_{\mathrm{GSMaP}}^{\mathrm{TS+}}$ relative to the SAR-derived RMW. The mean absolute error (MAE) is 14.1 km. After applying the outlier exclusion criterion (± 28.8 km), the error distribution fits a normal distribution reasonably well, with a standard deviation of 10.6 km.

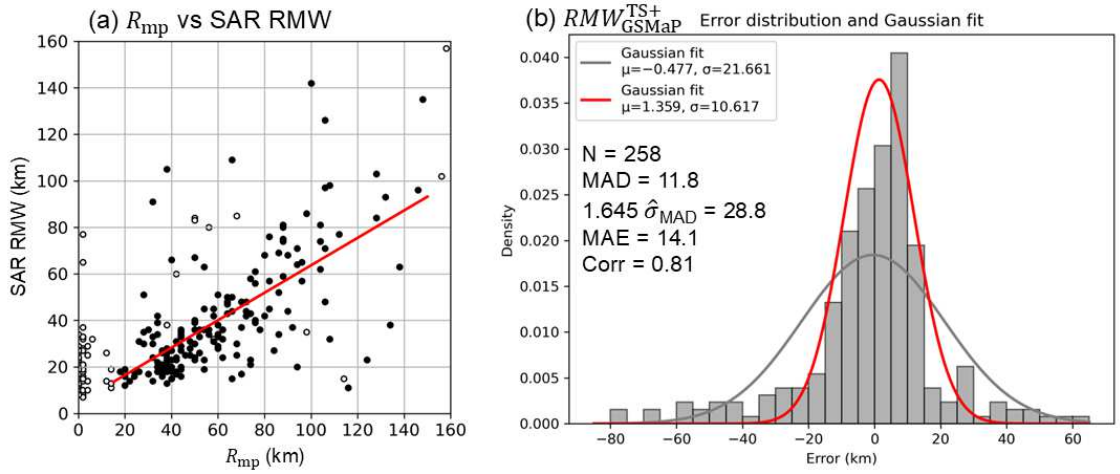


Fig. 1 (a) Scatter plot of R_{mp} (km) versus SAR-derived RMW (km). Black circles denote samples used in the regression (red line), and white circles denote excluded samples. (b) Distribution of $RMW_{\mathrm{GSMaP}}^{\mathrm{TS+}}$ errors (km), with Gaussian fits for all samples (gray) and for samples excluding outliers determined by a threshold value of 28.8 km (red). Sample size (N), median absolute deviation (MAD), criterion for outlier exclusion ($\pm 1.645\hat{\sigma}_{\mathrm{MAD}}$), mean absolute error (MAE), and correlation coefficient (Corr) are shown. MAE and Corr are calculated using all samples, including outliers.

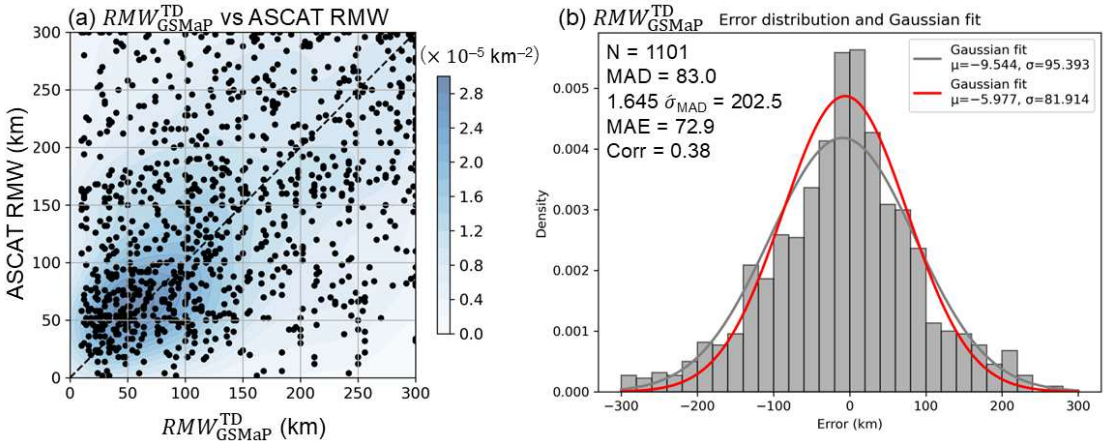
TD cases tend to have a local wind maximum within regions of strong precipitation. Accordingly, $RMW_{\mathrm{GSMaP}}^{\mathrm{TD}}$ is defined as follows:

i) Set $RMW_{\mathrm{GSMaP}}^{\mathrm{TD}} = R_{\mathrm{mp}}$ within 300 km, and identify the radius of maximum local precipitation, $R_{\mathrm{mp-local}}$.

ii) When $R_{\mathrm{mp}} < 10$ km, set $RMW_{\mathrm{GSMaP}}^{\mathrm{TD}} = R_{\mathrm{mp-local}}$ if $R_{\mathrm{mp-local}} \geq 10$ km; otherwise, set $RMW_{\mathrm{GSMaP}}^{\mathrm{TD}} = 10$ km.

iii) When $R_{\mathrm{mp}} = 300$ km and $R_{\mathrm{mp-local}} < 300$ km, set $RMW_{\mathrm{GSMaP}}^{\mathrm{TD}} = R_{\mathrm{mp-local}}$.

Figure 2 shows a scatter plot of $RMW_{\mathrm{GSMaP}}^{\mathrm{TD}}$ versus ASCAT-derived RMWs, along with the corresponding error distribution. The estimation errors are relatively large, reflecting not only the weak correlation between $RMW_{\mathrm{GSMaP}}^{\mathrm{TD}}$ and the RMW but also the uncertainties in the ASCAT-derived RMWs as reference data. This level of accuracy is considered unavoidable for TD cases.



315 **Fig. 2** (a) Scatter plot of $RMW_{\mathrm{GSMaP}}^{\mathrm{TD}}$ (km) versus ASCAT-derived RMW (km). The blue
316 shading indicates kernel density estimation ($\times 10^{-5}$ km^{-2}). (b) Distribution of
317 $RMW_{\mathrm{GSMaP}}^{\mathrm{TD}}$ errors (km), with Gaussian fits for all samples (gray) and for samples
318 excluding outliers determined by a threshold value of 202.5 km (red). Sample size (N),
319 median absolute deviation (MAD), criterion for outlier exclusion ($\pm 1.645\hat{\sigma}_{\mathrm{MAD}}$), mean
320 absolute error (MAE), and correlation coefficient (Corr) are shown. MAE and Corr are
321 calculated using all samples, including outliers.

322

323 ### 3.3 $RMW_{\mathrm{Rankine}}^{\mathrm{TS+}}$ and $RMW_{\mathrm{ERA5}}^{\mathrm{TD}}$

324 In RMW estimation methods based on precipitation distributions, center
325 displacement and the weak correspondence between asymmetric precipitation structures
326 and the low-level wind structure, particularly in cases exhibiting the shear pattern (Dvorak
327 1984), can be major sources of error. Therefore, this study develops a method to estimate
328 the RMW from a hypothetical radial wind profile constructed using bias-corrected ERA5
329 10-m wind fields, JMA V_{max}, and a modified Rankine vortex ($RMW_{\mathrm{Rankine}}^{\mathrm{TS+}}$) for TS
330 strength and above. In addition, a different method ($RMW_{\mathrm{ERA5}}^{\mathrm{TD}}$) is developed for cases
331 with $V_{\mathrm{max}} < 20$ m s^{-1} based on ERA5 10-m wind fields.

332

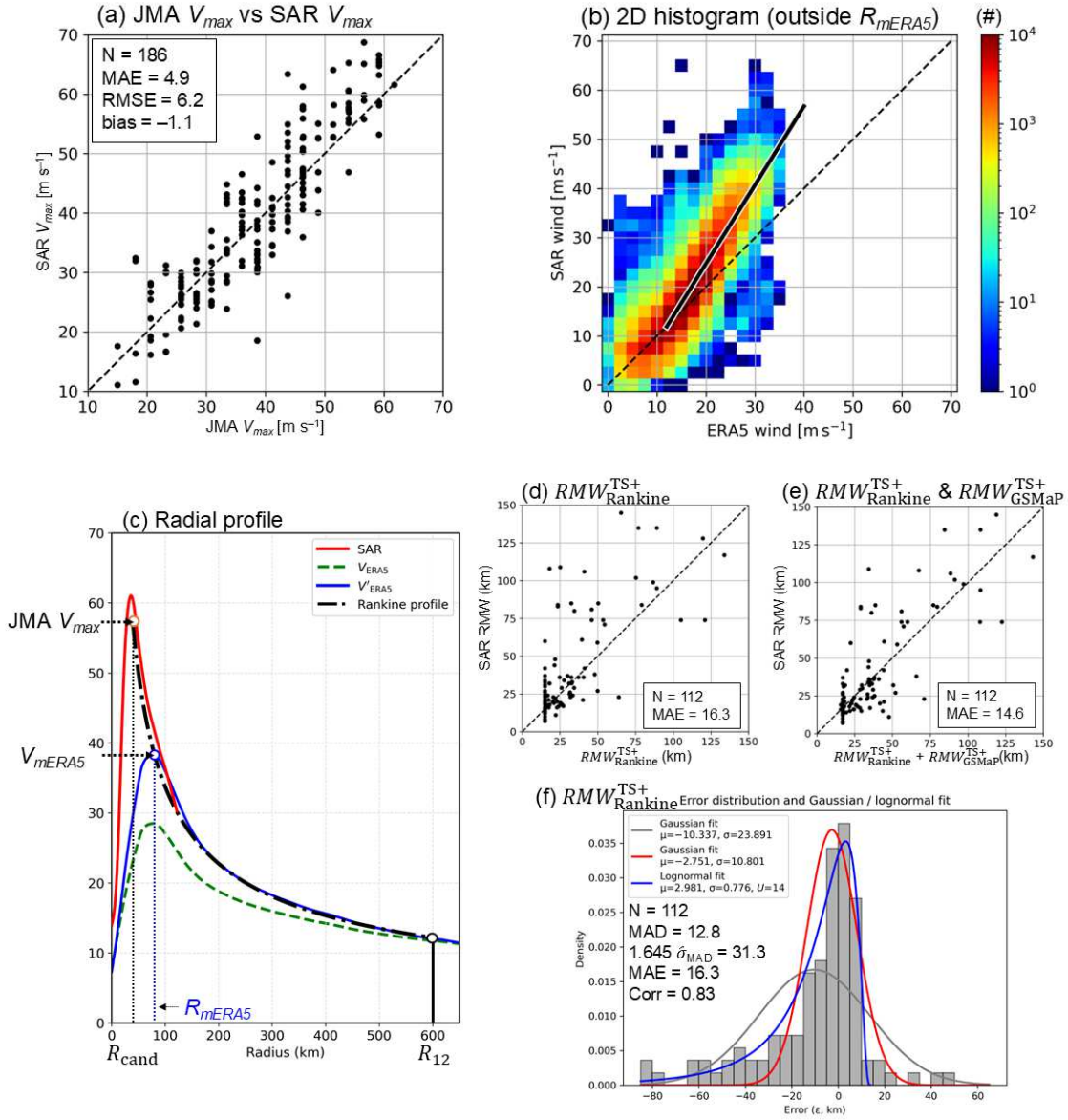


Fig. 3 (a) Scatter plot of JMA $V_{\max}$ (m s^{-1}) versus SAR-based $V_{\max}$ (m s^{-1}) derived from the azimuthally averaged wind speed. The dashed line denotes the 1:1 line. (b) Two-dimensional histogram of V_{ERA5} and SAR wind speeds sampled outside R_{mERA5}. The black line indicates the regression given by Eq. (3). (c) Example of radial profiles of the azimuthally averaged SAR wind speed (red), V_{ERA5} (green), V'_{ERA5} (blue), and the modified Rankine vortex (black) constructed using α determined from R_{12}, R_{mERA5}, and V_{mERA5}. (d) Scatter plot of $RMW^{\mathrm{TS+}}_{\mathrm{Rankine}}$ (km) versus SAR-derived RMW (km). (e) Scatter plot of the mean of $RMW^{\mathrm{TS+}}_{\mathrm{Rankine}}$ and $RMW^{\mathrm{TS+}}_{\mathrm{GSMaP}}$ (km) versus SAR-derived RMW (km). (f) Distribution of $RMW^{\mathrm{TS}}_{\mathrm{Rankine}}$ errors (km), with Gaussian and log-normal fits. Gaussian fits are derived from all samples (gray) and from samples excluding outliers determined by a threshold value of 31.3 km (red). The log-normal fit (blue) is derived

346 from samples with ε < 14.0 km (N = 106). Sample size (N), median absolute deviation
347 (MAD), criterion for outlier exclusion ($\pm 1.645\hat{\sigma}_{\mathrm{MAD}}$), mean absolute error (MAE), and
348 correlation coefficient (Corr) are shown. MAE and Corr are calculated using all samples,
349 including outliers. In (a–b), the samples are taken from the period 2015–2023, whereas
350 the samples in (d–f) are taken from the period 2015–2024.

351

352 For $RMW_{\mathrm{Rankine}}^{\mathrm{TS+}}$, the radial profile of the azimuthally averaged wind speed is
353 assumed, based on the theoretical framework of previous studies (Emanuel and Rotunno
354 2011; Chavas and Lin 2016), to be characterized by three parameters: the RMW, V_{max},
355 and the outer size. Here, the effect of latitude is neglected. Furthermore, the radial profile
356 approximately follows a modified Rankine vortex with an appropriate decay exponent α
357 (Mallen et al. 2005):

358
$$V(r) = \begin{cases} V_{\mathrm{max}} \dfrac{r}{RMW}, & r < RMW \\ V_{\mathrm{max}} \left(\dfrac{RMW}{r}\right)^{\alpha}, & r \geq RMW \end{cases}$$

359 where $V(r)$ denotes the axisymmetric wind speed at radius r. Based on these
360 assumptions, $RMW_{\mathrm{Rankine}}^{\mathrm{TS+}}$ is derived as follows:

361 i) JMA V_{max} is used because it is in good agreement with SAR V_{max} derived from the
362 azimuthally averaged wind speed (Fig. 3a).

363 ii) Because ERA5 wind speeds (V_{ERA5}) exceeding 12 m s^{-1} sampled outside the
364 RMW in the ERA5 wind field (R_{mERA5}) have a negative bias (Fig. 3b), the bias is
365 corrected linearly based on the comparison with SAR wind speeds (V'_{ERA5}, m s^{-}

[1]) as follows:

$$V'_{\mathrm{ERA5}} = 1.6\,V_{\mathrm{ERA5}} - 7.3, \qquad (V_{\mathrm{ERA5}} \geq 12.2). \tag{2}$$

The decay exponent α is then determined as:

$$\alpha = \frac{\log(V_{\mathrm{mERA5}}/12)}{\log(R_{12}/R_{\mathrm{mERA5}})},$$

where R_{12} denotes the innermost radius outside the RMW at which the azimuthally averaged V'_{ERA5} decreases to 12 m s^{-1}, and V_{mERA5} denotes $V_{\max}$ derived from the azimuthally averaged V'_{ERA5}.

iii) Wind speeds inside R_{mERA5} are extrapolated inward using the modified Rankine vortex profile with α determined in step (ii). The radius at which the extrapolated wind speed reaches JMA $V_{\max}$ is identified as a candidate RMW (R_{cand}; Fig. 3c). R_{cand} implies the following:

- Case A: for TCs with a single eyewall, R_{cand} is expected to approximately correspond to the true RMW; and
- Case B: for TCs with concentric eyewalls, R_{cand} may be located substantially outside the inner eyewall.

iv) Assuming Case A, $RMW^{\mathrm{TS+}}_{\mathrm{Rankine}} = R_{\mathrm{cand}}$ when $R_{\mathrm{cand}} < RMW^{\mathrm{TS+}}_{\mathrm{GSMaP}}$; otherwise, $RMW^{\mathrm{TS+}}_{\mathrm{Rankine}}$ is not defined. If $RMW^{\mathrm{TS+}}_{\mathrm{Rankine}} < 16$ km, reset $RMW^{\mathrm{TS+}}_{\mathrm{Rankine}} = 15$ km.

Although $RMW^{\mathrm{TS+}}_{\mathrm{Rankine}}$ alone does not achieve high accuracy (MAE = 16.3 km; Fig. 3d), nor does $RMW^{\mathrm{TS+}}_{\mathrm{GSMaP}}$ (MAE = 16.5 km), the mean of $RMW^{\mathrm{TS+}}_{\mathrm{Rankine}}$ and $RMW^{\mathrm{TS+}}_{\mathrm{GSMaP}}$ yields improved accuracy (MAE = 14.6 km; Fig. 3e). Accordingly, the inclusion of $RMW^{\mathrm{TS+}}_{\mathrm{Rankine}}$ in the consensus framework is expected to compensate for the weaknesses of $RMW^{\mathrm{TS+}}_{\mathrm{GSMaP}}$.

The estimation error ε of $RMW^{\mathrm{TS+}}_{\mathrm{Rankine}}$ exhibits a mode on the positive side and a negatively skewed tail in its frequency distribution (Fig. 3f). Therefore, this study adopts a log-normal distribution. The optimal value of U for $RMW^{\mathrm{TS+}}_{\mathrm{Rankine}}$ is set to 14 km. Outliers appear on both sides of the error ε with approximately uniform frequency.

In contrast to TS cases, TD cases generally do not have a modified Rankine vortex structure; therefore, a different approach is required. We found that the ERA5-derived RMWs tend, on average, to be located close to ASCAT-derived RMWs (Fig. 4a), likely because ERA5 assimilates ASCAT wind observations. In this study, the ERA5-derived RMW, $RMW^{\mathrm{TD}}_{\mathrm{ERA5}}$, is defined as follows:

i) Identify R_{mERA5} within 300 km of the TC center.

ii) When $R_{\mathrm{mERA5}} \leq 50$ km or $R_{\mathrm{mERA5}} = 300$ km, replace it with the radius of maximum local ERA5 wind speed. If the resulting radius is still less than 50 km, set $R_{\mathrm{mERA5}} = 50$ km.

iii) Finally, $RMW^{\mathrm{TD}}_{\mathrm{ERA5}}$ is obtained by applying a bias correction:

$$RMW^{\mathrm{TD}}_{\mathrm{ERA5}} = R_{\mathrm{mERA5}} - 34$$

The MAE of $RMW^{\mathrm{TD}}_{\mathrm{ERA5}}$ is 64.6 km (Fig. 4b), which is relatively large and comparable to that of $RMW^{\mathrm{TD}}_{\mathrm{GSMaP}}$ (Fig. 2). However, the consensus of $RMW^{\mathrm{TD}}_{\mathrm{GSMaP}}$ and $RMW^{\mathrm{TD}}_{\mathrm{ERA5}}$ reduces the MAE to 58.5 km.

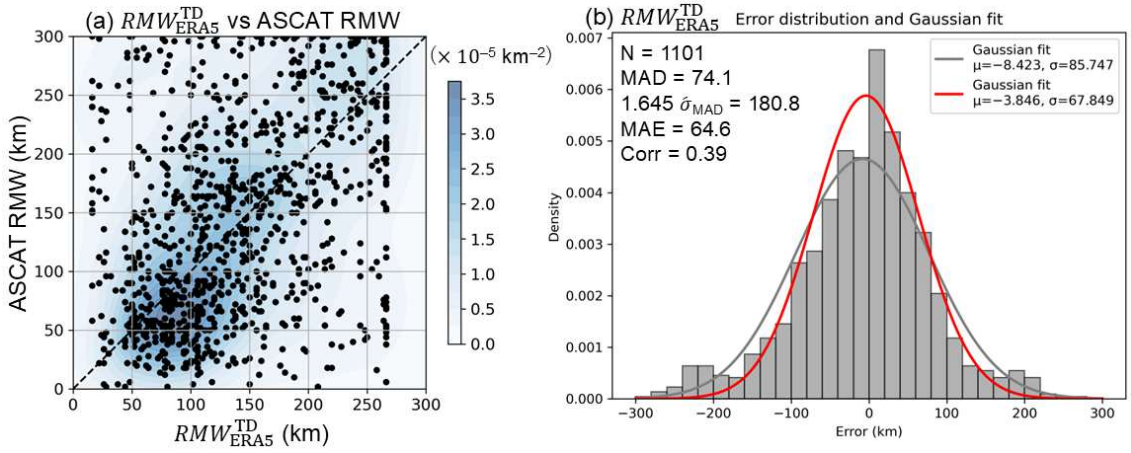


Fig. 4 (a) Scatter plot of $RMW^{\mathrm{TD}}_{\mathrm{ERA5}}$ (km) versus the ASCAT-derived RMW (km). The blue shading indicates kernel density estimation ($\times 10^{-5}$ km^{-2}). (b) Distribution of $RMW^{\mathrm{TD}}_{\mathrm{ERA5}}$ errors (km), with Gaussian fits for all samples (gray) and for samples excluding outliers determined by a threshold value of 180.8 km (red). Sample size (N), median absolute deviation (MAD), criterion for outlier exclusion ($\pm 1.645\hat{\sigma}_{\mathrm{MAD}}$), mean absolute error (MAE), and correlation coefficient (Corr) are shown. MAE and Corr are calculated using all samples, including outliers.

3.4 RMW_{IR}

The IR-based method developed by Tsukada and Horinouchi (2023) is adopted with some modifications. In this method, RMW_{IR} is estimated from R_{eye}, which is defined

as the radius of the minimum enclosing circle of the –45°C IR brightness temperature contour. To increase the availability of estimates, this study computes RMW_{IR} whenever the JMA Dvorak technique (Nishimura et al. 2023) indicates an "eye pattern," rather than restricting the estimation to cases classified as having a "clear eye," as in Tsukada and Horinouchi (2023). With these modifications, a new regression relationship is derived in this study:

$$RMW_{\mathrm{IR}} = 0.61R_{\mathrm{eye}} + 7.85$$

The MAE of RMW_{IR} is 4.6 km (Fig. 5a), which is larger than that reported by Tsukada and Horinouchi (2023). The error distribution of RMW_{IR} is well represented by a log-normal distribution, similar to that for $RMW^{\mathrm{TS}}_{\mathrm{Rankine}}$. The optimal value of U for the log-normal distribution of RMW_{IR} is 9 km.

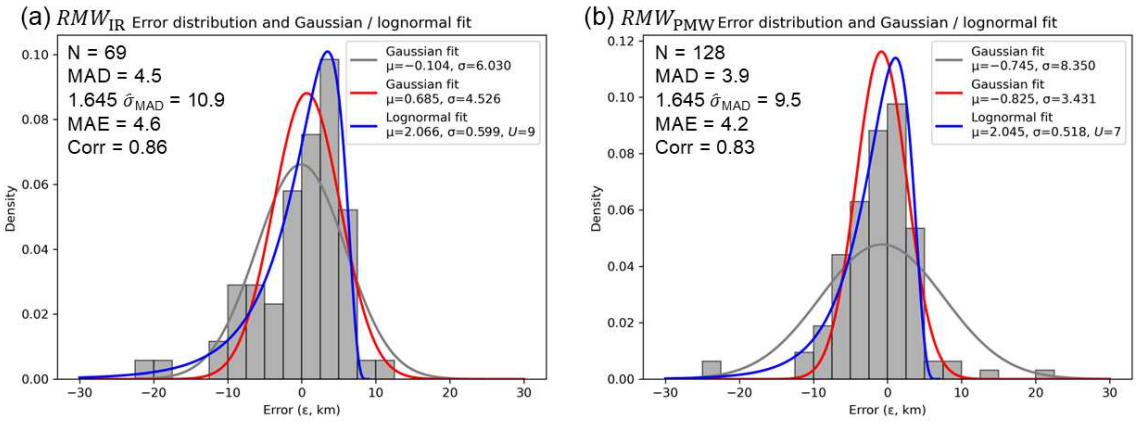


Fig. 5 (a) As in Fig. 3f, but for RMW_{IR} (km). The log-normal fit (blue) is derived from samples with ε < 9.0 km (N = 67). (b) As in Fig. 3f, but for RMW_{PMW} (km). The log-normal fit (blue) is derived from samples with ε < 7.0 km (N = 123).

3.5 RMW_{PMW}

The PMW-based method developed by Shimada (2025) is adopted using the following regression:

$$RMW_{\mathrm{PMW}} = 0.69R_{\mathrm{TB40}} + 6.11,$$

where R_{TB40} denotes the radius corresponding to the −40°C azimuthally averaged brightness temperature. Although Shimada (2025) proposed an additional estimation method, this study adopts only the above method for cases with JMA best track $V_{\max} > 33$ m s^{-1}, as the alternative method exhibits poorer accuracy than $RMW_{\mathrm{GSMaP}}^{\mathrm{TS+}}$. The MAE of RMW_{PMW} is 4.2 km (Fig. 5b). The error distribution of RMW_{PMW} is well represented by a log-normal distribution, with U = 7 km.

4 Consensus estimation

4.1 Bayesian consensus method

Bayes' theorem is applied to the consensus framework as follows:

$$p(X \mid x_1, x_2x_3, \ldots, x_T) = \frac{p(x_1, x_2x_3, \ldots, x_T \mid X)p(X)}{p(x_1, x_2x_3, \ldots, x_T)},$$

where the left-hand side represents the posterior probability density function (PDF) of the RMW, which is denoted by X, given the set of RMW estimates $\{x_1, x_2, x_3, \ldots, x_T\}$, with

452 T indicating the number of estimates. On the right-hand side, $p(x_1, x_2x_3, \ldots, x_T \mid X)$
453 denotes the likelihood of the estimates given X, and $p(X)$ denotes the prior PDF of X.
454 The denominator is a normalization constant. Error PDFs intrinsic to each estimation
455 method are used to compute the likelihood from the multiple estimates. Assuming
456 statistical independence among the estimates, the likelihood can be written as

457 $$p(x_1, x_2, \ldots, x_T|X) = \prod_i^T p(x_i|X).$$

458 In this study, the prior PDF of X is assumed to be uniform over $0 < X \leq 300$ km and
459 zero outside this range.

460 Under this assumption, the posterior PDF is proportional to the likelihood:

461 $$p(X \mid x_1, x_2x_3, \ldots, x_T) \propto \prod_i^T p(x_i|X), \qquad 0 < X \leq 300 \text{ km}. \tag{3}$$

462 Furthermore, in this study, each likelihood $p(x_i|X)$ is assumed to be the sum of an
463 error PDF and an outlier PDF, with the specific formulation given in the next subsection.
464 This formulation allows the likelihood to retain peaks near one or more of the individual
465 estimates (see the next subsection). The final RMW is obtained by evaluating the right-
466 hand side of Eq. (3) and is determined as the MAP estimate.

467 **4.2 Likelihoods**

468 The posterior PDF of the RMW is estimated with a radial resolution of 1 km by
469 evaluating the right-hand side of Eq. (3). Except for $RMW_{\text{GSMaP}}^{\text{TS+}}$ and $RMW_{\text{GSMaP}}^{\text{TD}}$, the

likelihoods of the RMW estimates are modeled as the sum of an error distribution represented by either a log-normal or a normal distribution with a weight of 90%, and an outlier distribution, assumed to be uniform over the range 0–300 km with a weight of 10%. The likelihoods of $RMW^{\mathrm{TS+}}_{\mathrm{GSMaP}}$ and $RMW^{\mathrm{TD}}_{\mathrm{GSMaP}}$ are described later. For each method, it is not easy to quantitatively estimate the outlier fraction because of the limited sample size. Nevertheless, all methods are expected to include outliers at some rate, as shown in Figs. 1–5.

For an estimate x_i (from $RMW^{\mathrm{TS}}_{\mathrm{Rankine}}$, RMW_{IR}, and RMW_{PMW}) whose errors are modeled by a log-normal distribution, the likelihood $p(x_i|X)$, with method-specific parameters σ_i, μ_i, and U_i (Table 1), is expressed as

$$p(x_i \mid X) = \frac{0.9}{\sqrt{2\pi}\sigma_i x'_i} \exp\left[-\frac{(\ln(x'_i) - \mu_i)^2}{2\sigma_i^2}\right] \mathbf{1}_{[0,\infty]}(x'_i) + \frac{0.1}{300}\mathbf{1}_{[0,300]}(x_i) \qquad (4)$$

where $x'_i = U_i - (x_i - X)$, $\mathbf{1}$ denotes the indicator function, and all radii are expressed in km. For an estimate x_i (from $RMW^{\mathrm{TD}}_{\mathrm{ERA5}}$) whose errors are modeled by a normal distribution, the likelihood $p(x_i|X)$, with a method-specific parameter σ_i (see Table 1), is expressed as

$$p(x_i|X) = \frac{0.9}{\sqrt{2\pi}\sigma_i} \exp\left[-\frac{(x_i - X)^2}{2\sigma_i^2}\right] + \frac{0.1}{300}\mathbf{1}_{[0,300]}(x_i) \qquad (5)$$

where all radii are expressed in km. The bias is assumed to be zero for simplicity.

By explicitly assuming an outlier distribution, the posterior distribution can be

multimodal, which helps avoid selecting a final RMW that is not supported by any individual method. To demonstrate this advantage, Fig. 6 shows an example of two posterior probability distributions obtained with and without an outlier distribution. Here, we suppose that there are four RMW estimates (22, 24, 58, and 62 km) forming two distinct clusters, with standard deviations of 5, 5, 10, and 10 km, respectively, for their error distributions. For simplicity, the error distributions are assumed to be normal distributions. Without an outlier distribution in the likelihood, the estimated posterior distribution is also a normal distribution, and the MAP estimate (30.4 km) lies between the two distinct clusters. In contrast, with an outlier distribution, the posterior distribution can be multimodal, with the MAP estimate (24.7 km) located close to one of the clusters.

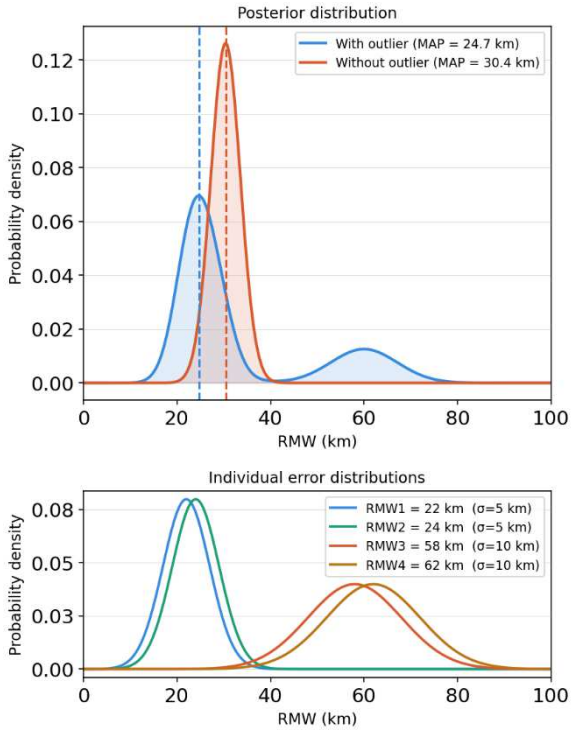


Fig. 6 (top) Posterior probability distributions obtained with and without an outlier distribution. (bottom) Individual error distributions corresponding to the RMW estimates.

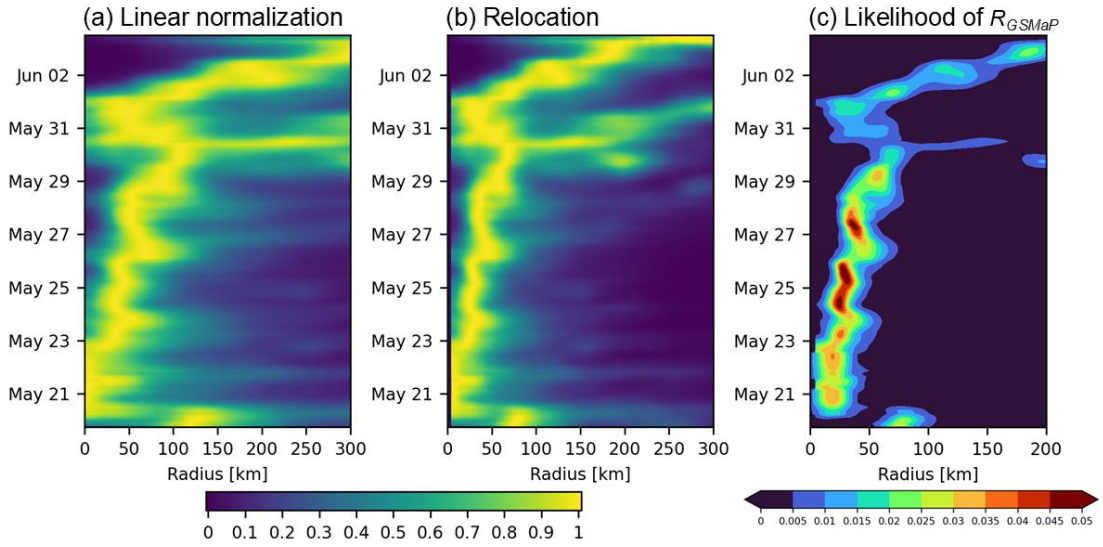


Fig. 7 Hovmöller diagrams of (a) linearly normalized precipitation, (b) relocated precipitation, and (c) the error distribution term of the $RMW_{\mathrm{GSMaP}}^{\mathrm{TS+}}$ likelihood for Typhoon Mawar (2023).

For the likelihoods of $RMW_{\mathrm{GSMaP}}^{\mathrm{TS+}}$ and $RMW_{\mathrm{GSMaP}}^{\mathrm{TD}}$, additional modifications are introduced. In the estimation of $RMW_{\mathrm{GSMaP}}^{\mathrm{TS+}}$ and $RMW_{\mathrm{GSMaP}}^{\mathrm{TD}}$, a single radius must be selected as R_{mp} [Eq. (1)]. However, in cases with concentric eyewalls, pronounced asymmetries, or broad radial wind profiles, potential RMWs may be distributed over a wider range of radii than in single-eyewall cases. In such situations, the error distribution term of the $RMW_{\mathrm{GSMaP}}^{\mathrm{TS+}}$ and $RMW_{\mathrm{GSMaP}}^{\mathrm{TD}}$ likelihoods cannot be assumed to follow a normal distribution and is therefore constructed instead from the radial distribution of azimuthally averaged precipitation normalized by its maximum value (Fig. 7a). Since

$RMW_{\mathrm{GSMaP}}^{\mathrm{TS+}}$ is originally derived from the radius of maximum precipitation, the normalized precipitation is relocated (Fig. 7b) using an equation consistent with Eq. (1): $r' = 0.59\,r + 4.68$, where r' is the relocated radius. The peak of the relocated precipitation is then enhanced to obtain the final distribution (Fig. 7c). More specific procedures for the error distributions of $RMW_{\mathrm{GSMaP}}^{\mathrm{TS+}}$ and $RMW_{\mathrm{GSMaP}}^{\mathrm{TD}}$ are given in Appendix B. Finally, the $RMW_{\mathrm{GSMaP}}^{\mathrm{TS+}}$ and $RMW_{\mathrm{GSMaP}}^{\mathrm{TD}}$ likelihoods also include a uniform outlier distribution, as in Eq. (4).

4.3 Estimation procedure

As consensus members, all RMW estimates available at each analysis time are used. In addition, when RMW_{IR} or RMW_{PMW}, which has high accuracy but limited availability, is not available at a given analysis time, (i) the estimate from 3 h prior to the analysis time, or otherwise (ii) the estimate from 3 h after the analysis time, is included as a consensus member, if available. Consequently, the same RMW_{IR} or RMW_{PMW} estimates can be used in the consensus for up to three consecutive analysis times.

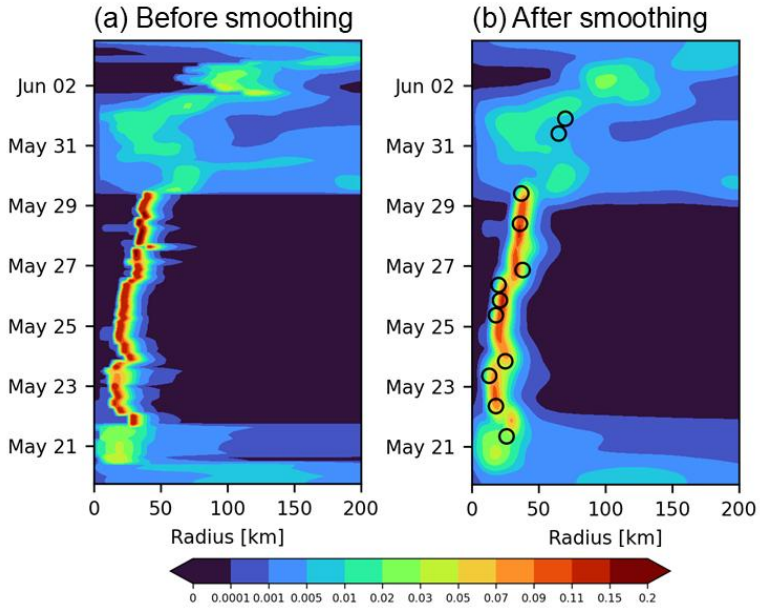


Fig. 8 Hovmöller diagrams of the posterior probability distribution of the RMW (a) before and (b) after smoothing for Typhoon Mawar (2023).

After the posterior distribution is computed, a 1-1-1 filter is applied to it in both the radial and temporal directions to suppress irregular fluctuations (Fig. 8). The filter is applied iteratively five times, as determined empirically, enabling the RMW to evolve smoothly over time (Fig. 8b).

The final RMW is determined by the MAP estimate [i.e., $\arg\max_X p(X \mid x_1, x_2 x_3, \ldots, x_T)$]. However, spike-like fluctuations occasionally remain in the temporal evolution of the final RMW. Such residual spikes are identified and corrected at each analysis time t as follows. Define $\Delta RMW1 = RMW(t) - RMW(t-3h)$ and $\Delta RMW2 = RMW(t+3h) - RMW(t)$. If $|\Delta RMW1| > 10$ km, $|\Delta RMW2| > 10$ km, $\Delta RMW1 * \Delta RMW2 <$

0, and $\min\left(\frac{|\Delta RMW1|}{|\Delta RMW2|}, \frac{|\Delta RMW2|}{|\Delta RMW1|}\right) > 0.2$, then the $RMW(t)$ is replaced by the average of $RMW(t-3h)$ and $RMW(t+3h)$. This procedure is applied iteratively three times.

5 Verification

Verification of the consensus RMW estimates is conducted using matchup samples with SAR observations. Since SAR-derived RMWs during the period 2015–2024 are used to develop the individual RMW estimation methods in Sect. 3, the matchup samples are divided into dependent samples from 2015–2024 and independent samples from 2025. Here, SAR scenes with concentric eyewalls are included. Two case studies are then presented.

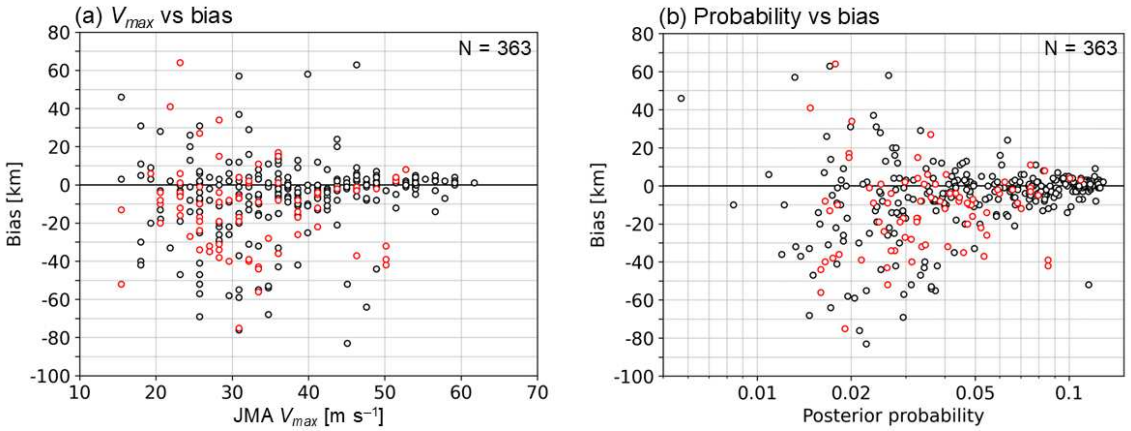
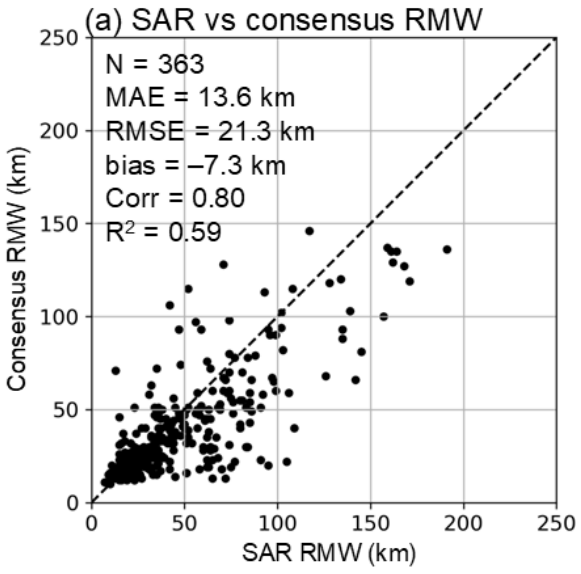
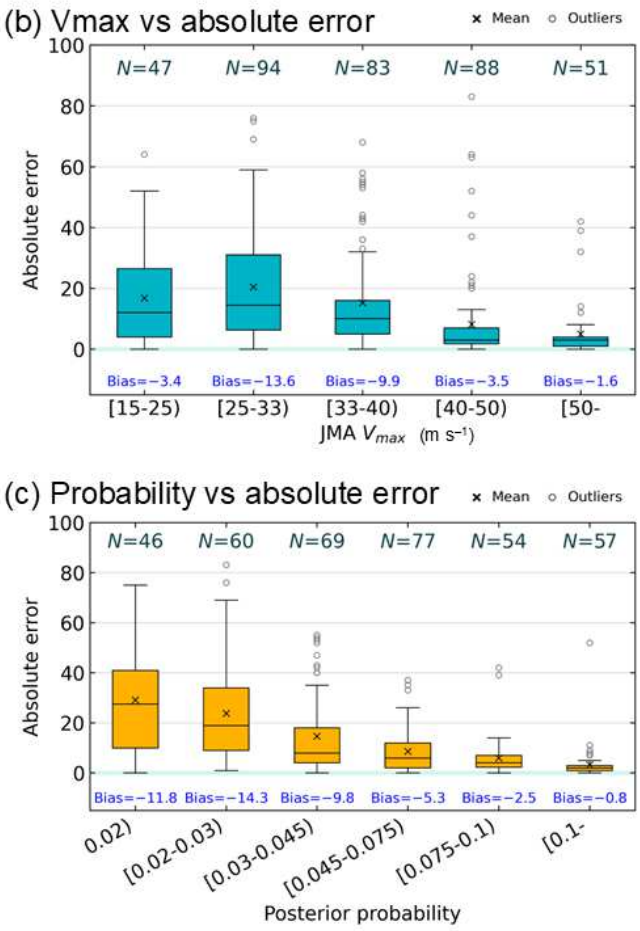


Fig. 9 Relationships between (a) JMA $V_{\max}$ (m s^{-1}) and bias (consensus minus SAR-derived RMW; km) and (b) posterior probability and bias (km). Black circles denote dependent samples, and red circles denote independent samples.

Figure 9 shows the bias of the consensus RMW estimates as a function of JMA $V_{\max}$

and the peak posterior probability. There is little difference in the error distributions between dependent and independent samples. Errors decrease with increasing V_{max} and with increasing posterior probability. Weak TCs tend to have poorly defined structures, making RMW estimation difficult and causing larger estimation errors for $V_{max} < 35$ m s^{-1}. Additionally, seven of the nine samples with $V_{max} > 40$ m s^{-1} and large errors (> 30 km) are associated with concentric eyewalls. For such cases, large errors can occur if the estimated RMW is associated with the inner eyewall while the true RMW corresponds to the outer eyewall, or vice versa. A more distinct relationship is found between the error and the posterior probability, with errors being smaller for posterior probabilities > 0.04. Therefore, the posterior probability itself can serve as an indicator of the reliability of the RMW estimates.



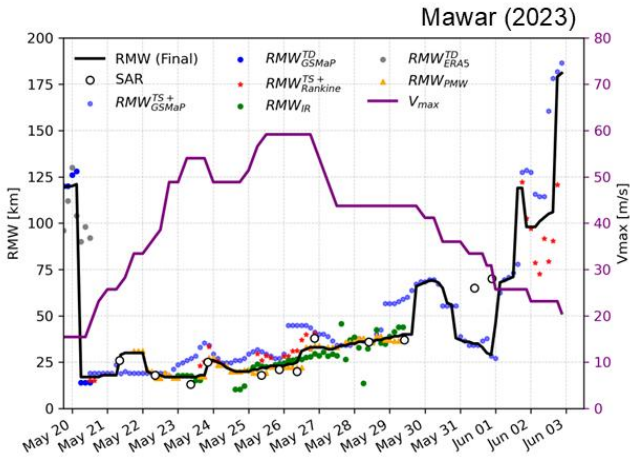


570

571 **Fig. 10** (a) Scatter plot of SAR-derived RMW (km) versus consensus RMW (km). The
572 dashed line denotes the 1:1 line. Sample size (*N*), mean absolute error (MAE), root-mean-
573 square error (RMSE), bias, correlation coefficient (Corr), and coefficient of determination
574 R^2 are shown. (b–c) Boxplots of absolute errors stratified by JMA V_{max} (m s^{-1}) and
575 posterior probability, respectively. A cross denotes the MAE for each group, and circles
576 denote outliers. Sample size (*N*) and bias are shown.

577

578 The MAE calculated using both dependent and independent samples is 13.7 km (Fig.
579 10a). A negative bias is evident, particularly for 25 m s^{-1} ≤ V_{max} < 40 m s^{-1} (Fig. 10b) and
580 for posterior probabilities < 0.045 (Fig. 10c). Although the errors are widely distributed,
581 62% of the samples have absolute errors of ≤ 10 km (not shown).



582

583 **Fig. 11** Temporal evolution of the consensus RMW estimates (thick black line) together
584 with the individual estimates for Typhoon Mawar (2023). White circles denote SAR-
585 derived RMWs as reference.

586

587 Figure 11 shows the temporal evolution of the consensus RMWs together with the
588 individual estimates for Typhoon Mawar (2023), as a representative case of an intense
589 TC. The consensus primarily follows $RMW^{\mathrm{TS+}}_{\mathrm{GSMaP}}$, with appropriate corrections from
590 RMW_{IR} and RMW_{PMW} when available. The comparison with the SAR-derived RMWs
591 shows that the consensus successfully determines appropriate RMW estimates. Figure 8b
592 shows a Hovmöller diagram of the posterior probability distribution for Mawar. Mawar
593 is characterized by sharply peaked distributions during periods with a well-defined eye,
594 whereas broader distributions appear during its initial and decaying stages. The rapid
595 outward shift of the radius of maximum posterior probability suggests that eyewall
596 replacement cycles (ERCs) occurred at least twice, at ~1800 UTC 23 May and ~1200
597 UTC 26 May. Furthermore, the posterior distribution agrees closely with SAR-derived

RMWs when the distribution is sharply peaked, whereas discrepancies increase when it is broad. Therefore, the posterior distribution obtained by the consensus method is useful not only for RMW estimation but also for assessing its reliability and diagnosing ERCs.

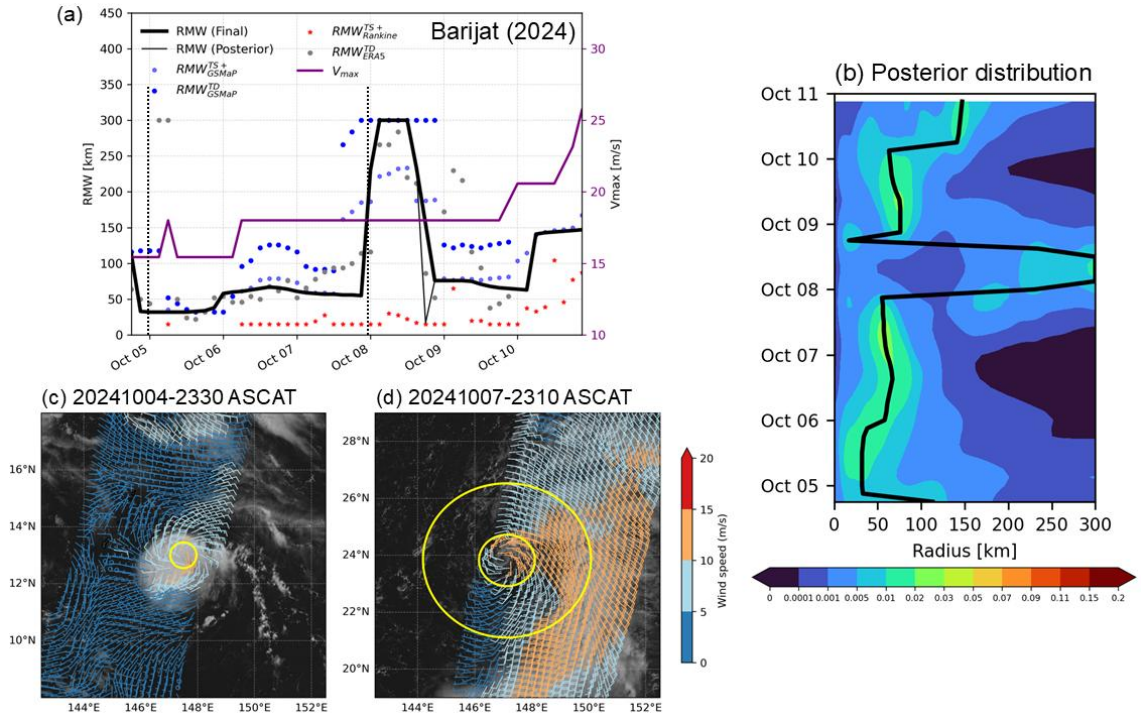


Fig. 12 (a) As in Fig. 11, but for Tropical Storm Barijat (2024). Vertical lines indicate the times shown in (c) and (d). The V_{max} of 18 m s^{-1} at 0600 UTC 5 October results from extrapolation during the TD stage (see Sect. 2). (b) Hovmöller diagram of the posterior probability distribution of the RMW. The thick black line denotes the radius of maximum posterior probability. (c–d) ASCAT wind fields at ~2330 UTC 4 October and ~2310 UTC 7 October, respectively, with the corresponding visible imagery overlaid. The yellow circles indicate a radius of 50 km in (c), and radii of 100 km and 300 km in (d). In (d), the TC center in the ASCAT wind field appears displaced from that in the visible imagery, possibly due to the coarse spatial resolution of ASCAT (25 km).

Figure 12 shows Tropical Storm Barijat (2024) as a representative case of a weak TC. A spike-like fluctuation in the MAP estimate at 1800 UTC 8 October is corrected by the

post-processing procedure (Fig. 12a). In general, RMW estimation is difficult for weak TCs (e.g., Shimada 2025). This case exhibits a broad posterior distribution (Fig. 12b), suggesting large estimation uncertainty. Because the ERA5 wind field of Barijat exhibits a small-sized vortex throughout its life cycle (not shown), $RMW^{\mathrm{TS}}_{\mathrm{Rankine}}$ remains small as well, mostly below 30 km. There are two noticeable features of the RMW estimates for Barijat. First, the RMW is estimated to be less than 30 km during the initial TD period, which is smaller than that during the TS period. The ASCAT wind field shows a small vortex with a possible RMW of less than 50 km (Fig. 12c), indicating that the consensus RMW estimates are reasonable. Second, the consensus RMW reaches 300 km (the maximum possible value in this method) on 8 October. The ASCAT observations and visible imagery show a small low-level vortex without deep convection in its vicinity, along with a relatively strong wind region on the eastern side of the TC (Fig. 12d), representing a typical "shear pattern" in the Dvorak technique. $RMW^{\mathrm{TS}}_{\mathrm{Rankine}}$ corresponds to the RMW of the small-sized low-level vortex, whereas $RMW^{\mathrm{TS+}}_{\mathrm{GSMaP}}$ corresponds to the strong wind region on the eastern side. These two potential RMWs are appropriately reflected in the posterior distribution.

6 Long-term dataset

A long-term RMW dataset is constructed for TCs that occurred in the western North Pacific since 2000, because GSMaP data with homogeneous quality have been available from that year onward. A total of 631 TCs during the period 2000–2025 are included in the dataset. The RMW is estimated at 3-h intervals for periods during which the JMA best track data classify the TCs as TDs or stronger. The dataset includes the consensus RMW, the posterior probability at the RMW, the posterior probability distribution, as well as the RMW estimates from the available methods (Shimada and Tsukada 2026).

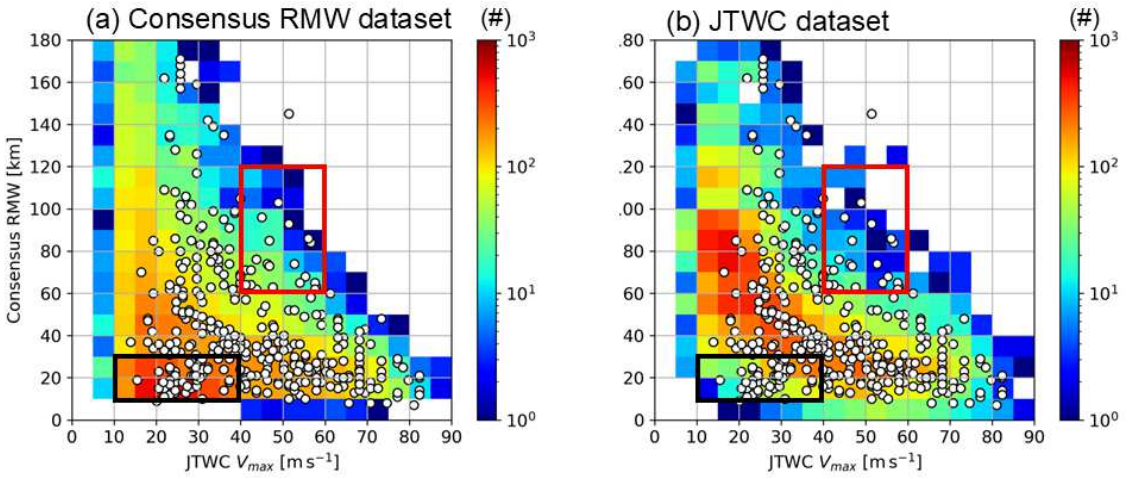


Fig. 13 Two-dimensional histograms of 6-hourly (a) JTWC $V_{\max}$ (m s^{-1}) versus consensus RMW (km) and (b) JTWC $V_{\max}$ (m s^{-1}) versus JTWC best track RMW (km) during 2001–2025. White circles denote SAR-derived RMWs and their corresponding JTWC $V_{\max}$ values during 2015–2025. Black and red boxes indicate areas I and II, respectively.

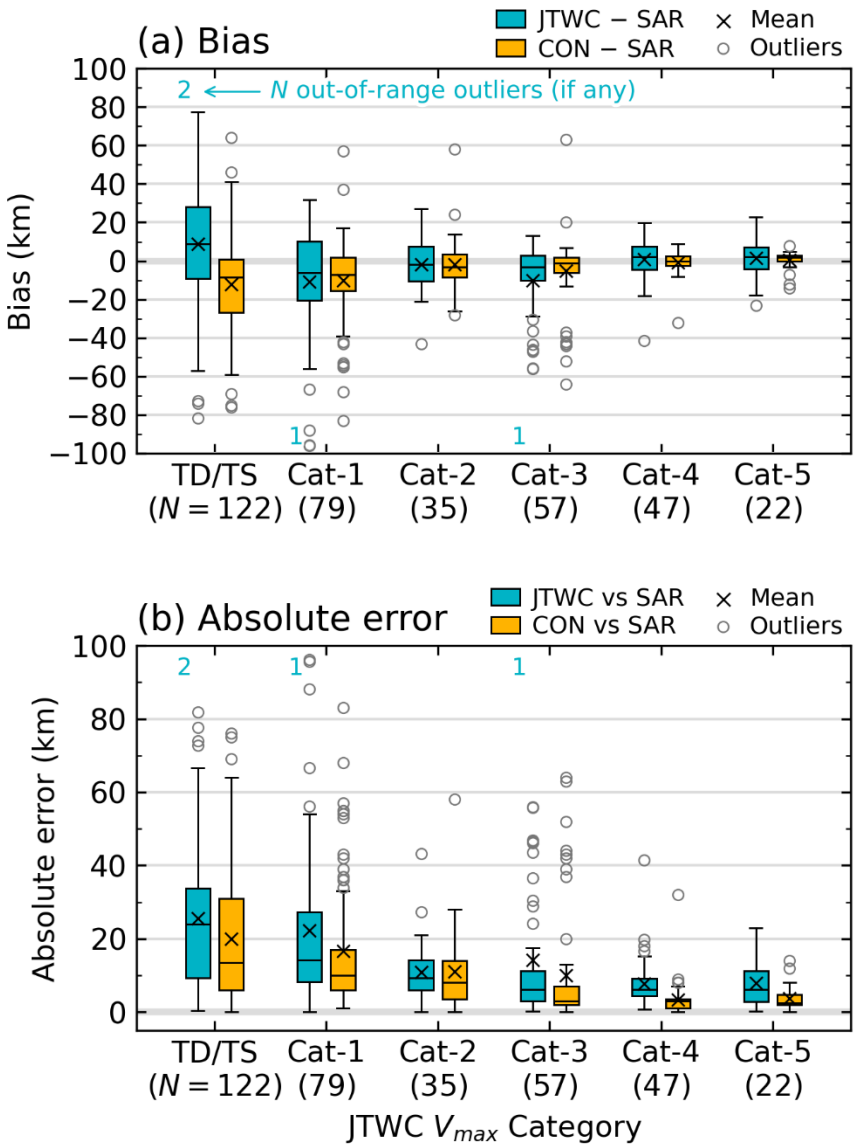


Fig. 14 Boxplots of (a) bias and (b) absolute error of JTWC and consensus RMWs against SAR-derived RMWs, stratified by Saffir-Simpson hurricane wind scale categories based on JTWC $V_{\max}$. A cross denotes the MAE for each group, and circles denote outliers. Sample size (N) is shown below the category name. The numbers indicated in teal represent out-of-range outliers beyond ± 100 km.

Figure 13 shows the two-dimensional histogram of the JTWC best track $V_{\max}$ and the consensus RMW for the period 2001–2025, in comparison with the corresponding JTWC

654 best track RMW[1] (Howell et al. 2025). The consensus RMW dataset shows a frequency
655 distribution that differs from the JTWC RMW dataset. In particular, pronounced
656 differences are found in two regions: area I, defined by V_{max} = 10–40 m s^{-1} and RMW =
657 12.5–35.0 km, and area II, defined by V_{max} = 40–60 m s^{-1} and RMW = 60–120 km. Area
658 I is characterized by the absence of a distinct frequency peak in the JTWC RMW dataset,
659 whereas a clear frequency peak appears in each V_{max} bin in the consensus RMW dataset.
660 The presence of these frequency peaks is consistent with SAR observations for cases with
661 V_{max} > 20 m s^{-1}, although further verification is needed because the consensus RMWs for
662 weak storms tend to have negative biases (Fig. 10b). Area II is characterized by very few
663 samples in the JTWC RMW dataset, but by moderate frequencies in the consensus RMW
664 dataset, in agreement with SAR observations. In reality, cases with V_{max} ≈ 50 m s^{-1} and
665 RMW ≈ 100 km have been observed (e.g., Typhoon Trami 2018; Hirano et al. 2022),
666 suggesting that the consensus RMW dataset is capable of realistically representing a wide
667 range of RMW values.

668 Figure 14 compares the bias and absolute error of the JTWC and consensus RMWs
669 against SAR-derived RMWs. The consensus RMW dataset generally has a narrower
670 range of boxplot whiskers for both bias and absolute error. In particular, both the mean

[1] JTWC best track RMWs have been included in the dataset since 2001.

and median of the absolute error are smaller for the consensus RMWs than for the JTWC RMWs, indicating that the consensus RMW dataset has better accuracy. Note that the JTWC RMW values included in the best track dataset are not reanalyzed after the season and have been estimated without SAR observations, except in very recent years (Howell et al. 2025). Furthermore, very small and large RMW estimates tend to be avoided for use in TC vitals and guidance suites. These factors likely contribute to the large difference in RMWs between the consensus and JTWC datasets.

The new RMW dataset may alter the climatology of TC RMWs in the western North Pacific. In particular, since this dataset extends back to the 2000s, a period during which SAR observations were unavailable, the representation of small RMWs, which may not have been captured in previous datasets and studies, is expected to be substantially improved. A detailed evaluation and further analyses will be conducted in a future study.

7 Summary

Given the importance of RMW information for a wide range of applications, there is a need to develop new techniques and to construct a long-term, homogeneous RMW dataset (Rogers et al. 2023; Ito et al. 2025). Although multiple RMW estimates using different methods have been available for the same analysis time based on previous

689 studies, no consensus method suitable for RMW estimation has been developed to obtain
690 a single RMW estimate from multiple estimates.

691 To this end, this study develops a consensus method based on a Bayesian framework.
692 In the consensus approach, the posterior probability distribution of the RMW given
693 multiple RMW estimates is estimated using likelihoods constructed from method-specific
694 error distributions combined with an outlier distribution, and the final RMW is
695 determined as the MAP estimate. By explicitly accounting for an outlier distribution, the
696 consensus method can appropriately determine a reasonable RMW close to one of the
697 clusters even when the estimates split into two distinct clusters.

698 Using this method, we construct a long-term RMW dataset at 3-h intervals for 631
699 TCs in the western North Pacific during 2000–2025. As consensus members, the input
700 estimates include those from methods using a satellite-based global precipitation dataset
701 ($RMW^{\mathrm{TS+}}_{\mathrm{GSMaP}}$ and $RMW^{\mathrm{TD}}_{\mathrm{GSMaP}}$), methods based on IR and PMW satellite data when an
702 eye is observed (RMW_{IR} and RMW_{PMW}), a modified Rankine vortex method
703 ($RMW^{\mathrm{TS+}}_{\mathrm{Rankine}}$), and an ERA5-based method ($RMW^{\mathrm{TD}}_{\mathrm{ERA5}}$). Verification of the consensus
704 RMW estimates shows that errors decrease with increasing TC intensity and posterior
705 probability, and that the posterior probability itself serves as an indicator of estimate
706 reliability. This new RMW dataset enables a more realistic representation of the inner-

core structure, particularly for small RMWs that were difficult to estimate without aircraft observations before the advent of SAR-derived winds.

Because the proposed Bayesian consensus method allows the incorporation of any available estimates with their associated error characteristics, observation-derived RMWs, such as those obtained from SAR, ASCAT, and L-band radiometers, can also be included in the consensus framework, in addition to the RMW estimates used in this study, if long-term homogeneity of the final RMW estimates is not strictly required. Incorporating such additional RMWs would likely further reduce the overall estimation error compared with that of the dataset constructed in this study and would be useful for operational applications. Although this study focuses on TCs in the western North Pacific, the proposed framework can be readily applied to TCs worldwide. This extension is left for future work. The proposed framework provides a practical basis for improving RMW estimation and supporting both research and operational applications.

Acknowledgements

U. Shimada is deeply grateful to his colleagues at MRI and JMA Headquarters for their encouragement and fruitful discussions. The views expressed in this paper are those of the authors and should not be regarded as official JMA views. U. Shimada was supported

by the Japan Society for the Promotion of Science (JSPS) KAKENHI Grant 23K13172 and the Japan Science and Technology Agency (JST) Moonshot JPMJMS2282. This paper is also supported by the collaborative research program (2025GC-06) of the Disaster Prevention Research Institute of Kyoto University. T. Tsukada was supported by the Cooperative Institute for Research in the Atmosphere (CIRA) and National Oceanic and Atmospheric Administration (NOAA) under Cooperative Agreement NA24OARX432C0007.

Appendix A

List of the notation used in this paper.

R_{12}	Radius of the 12 m s^{-1} azimuthally averaged V'_{ERA5}.
R_{TB40}	Radius of the azimuthally averaged brightness temperature at −40°C.
R_{cand}	Candidate RMW.
R_{eye}	Radius of the minimum enclosing circle of the –45°C IR brightness temperature contour.
R_{mERA5}	RMW derived from the ERA5 wind field.
R_{mp}	Radius of maximum azimuthally averaged precipitation within 300 km of the TC center.
R_{mp1}, R_{mp2}, R_{mp3}	The first, second, and third peaks of the azimuthally averaged precipitation beyond a radius of 10 km.
$R_{\mathrm{mp-local}}$	Radius of maximum local precipitation.
$RMW^{\mathrm{TD}}_{\mathrm{ERA5}}$	RMW estimate using ERA5 wind data for TD strength.
$RMW^{\mathrm{TD}}_{\mathrm{GSMaP}}$	RMW estimate using GSMaP data for TD strength.
$RMW^{\mathrm{TS+}}_{\mathrm{GSMaP}}$	RMW estimate using GSMaP data for TS strength and above.
RMW_{IR}	RMW estimate using IR satellite data.
RMW_{PMW}	RMW estimate using PMW satellite data.

$RMW^{\mathrm{TS+}}_{\mathrm{Rankine}}$	RMW estimate using a modified Rankine vortex profile and ERA5 wind data for TS strength and above.
V_{ERA5}	ERA5 10-m wind speeds.
V'_{ERA5}	Bias-corrected V_{ERA5}.
V_{mERA5}	$V_{\max}$ derived from the azimuthally averaged V'_{ERA5}.

735

736 **Appendix B**

737 The error distribution term of the $RMW^{\mathrm{TS+}}_{\mathrm{GSMaP}}$ and $RMW^{\mathrm{TD}}_{\mathrm{GSMaP}}$ likelihoods is
738 specifically derived as follows:

739 i) Linearly normalize the 12-h running mean precipitation in step (i) of section 3.2
740 by its maximum value within a radius of 400 km from the TC center at each time
741 (Fig. 7a).

742 ii) Relocate the normalized precipitation using an equation consistent with Eq. (1):

743 $$r' = 0.59\,r + 4.68$$

744 where r' is the relocated radius (Fig. 7b). For example, precipitation originally
745 located at r = 100 km is relocated to r' = 63.68 km.

746 iii) Further normalize the precipitation relocated in step (ii) to follow a normal-
747 distribution-shaped function defined as

748 $$PR_{\mathrm{nml}} = \exp\left[-\frac{(1-PR')^2}{2\sigma^2_{\mathrm{nml}}}\right]$$

749 where PR' is the normalized precipitation derived in step (i), and σ_{nml} = 0.3.

The value of σ_{nml} is chosen so that the maximum likelihood derived in step (v) becomes comparable to those of other methods (0.03–0.1). This normalization is necessary because the PR' distribution yields a maximum likelihood of only ~0.01, which is much smaller than those of other methods (Figs. 3f and 5).

iv) Apply a correction to the PR_{nml} distribution to address the constraint that $RMW_{\mathrm{GSMaP}}^{\mathrm{TS+}}$ is set to 19 km when $R_{\mathrm{mp}} < 16$ km (Sect. 3.2). Here, the derivation of R_{mp} follows the same procedures as in Sect. 3.2, except for step (iii), which is redefined as follows: When $R_{\mathrm{mp}} < 10$ km, compute the radius of maximum azimuthally averaged precipitation prior to applying a 12-h running mean ($R_{\mathrm{mp}}^{\mathrm{pre}}$), and set R_{mp} to the smaller of R_{mp1} and $R_{\mathrm{mp}}^{\mathrm{pre}}$ that lies between 10 km and 40 km; if no such value exists, R_{mp} remains unchanged. Then, the PR_{nml} distribution is corrected as follows:

- When $R_{\mathrm{mp}} < 16$ km:

$$PR_{\mathrm{nml}} = \begin{cases} \exp\left[-\dfrac{(r-\mu)^2}{2\sigma^2}\right], & r \le 19 \text{ km} \\ \max\left(\exp\left[-\dfrac{(r-\mu)^2}{2\sigma^2}\right], PR_{\mathrm{nml}}\right), & r > 19 \text{ km} \end{cases} \quad (B1)$$

where μ = 19 km and σ = 10.617, corresponding to the standard deviation of the $RMW_{\mathrm{GSMaP}}^{\mathrm{TS+}}$ error distribution (Table 1).

- When $R_{\mathrm{mp}} \ge 16$ km:

767 $$PR_{\mathrm{nml}} = \begin{cases} y_0 \exp\left[-\dfrac{(r-\mu)^2}{2\sigma^2}\right], & r \le 15\ \mathrm{km} \\ PR_{\mathrm{nml}}, & r > 15\ \mathrm{km} \end{cases} \quad (B2)$$

768 where $y_0 = PR_{\mathrm{nml}}$ evaluated at r = 14 km in step (iii), μ = 14 km, and σ

769 is the same as that defined above.

770 v) Divide the PR_{nml} distribution by its sum over the range 0–300 km to obtain the

771 error distribution term of the $RMW^{\mathrm{TS+}}_{\mathrm{GSMaP}}$ likelihood (Fig. 7c).

772 For the error distribution term of the $RMW^{\mathrm{TD}}_{\mathrm{GSMaP}}$ likelihood, step (i) above is

773 applied to obtain PR_{nml}. Steps (ii) and (iii) are skipped. In step (iv), when $R_{\mathrm{mp}} < 20$ km,

774 the same correction as Eq. (B1) is applied. When $R_{\mathrm{mp}} \ge 20$ km, a correction based on

775 Eq. (B2) with μ = 19 km is applied for $r \le 19$ km. Step (v) is then applied. The

776 maximum likelihood is less than ~0.01, which is comparable to that of $RMW^{\mathrm{TD}}_{\mathrm{ERA5}}$ (not

777 shown).

778

779 **References**

780 Aijaz S, Kepert JD, Ye H, Huang Z, Hawksford A (2019) Bias correction of tropical

781 cyclone parameters in the ECMWF ensemble prediction system in Australia. Mon

782 Weather Rev 147:4261–4285. https://doi.org/10.1175/MWR-D-18-0377.1

783 Aizawa M, Ito K, Shimada U (2024) Revisiting Koba's relationship to improve minimum

784 sea-level pressure estimates of western North Pacific tropical cyclones. J Meteorol

Soc Japan 102:377–390. https://doi.org/10.2151/jmsj.2024-018

Avenas A, Mouche A, Tandeo P, Piolle J, Chavas D, Fablet R, Knaff J, Chapron B (2023) Reexamining the estimation of tropical cyclone radius of maximum wind from outer size with an extensive synthetic aperture radar dataset. Mon Weather Rev 151:3169–3189. https://doi.org/10.1175/MWR-D-22-0277.1

Avenas A, Tsukada T, Cévaër T, Knaff J, Mouche A, Chapron B (2026) The global kilometric tropical cyclone wind database (CyclObs) enabling high-resolution data-driven studies. Submitted to Bull Am Meteorol Soc. https://doi.org/10.1175/MWR-D-22-0277.1

Bessho K, et al (2016) An introduction to Himawari-8/9—Japan's new-generation geostationary meteorological satellites. J Meteorol Soc Japan 94:151–183. https://doi.org/10.2151/jmsj.2016-009

Black ML, Willoughby HE (1992) The concentric eyewall cycle of Hurricane Gilbert. Mon Weather Rev 120:947–957. https://doi.org/10.1175/1520-0493(1992)120<0947:TCECOH>2.0.CO;2

Carrasco C, Landsea C, Lin Y (2014) The influence of tropical cyclone size on its intensification. Weather Forecast 29:582–590. https://doi.org/10.1175/WAF-D-13-00092.1

803 Chavas DR, Knaff JA (2022) A simple model for predicting the tropical cyclone radius of
804 maximum wind from outer size. Weather Forecast 37:563–579.
805 https://doi.org/10.1175/WAF-D-21-0137.1
806 Chavas DR, Lin N (2016) A model for the complete radial structure of the tropical cyclone
807 wind field. Part II: Wind field variability. J Atmos Sci 73:3093–3113.
808 https://doi.org/10.1175/JAS-D-15-0014.1
809 Chen B-F, Chen C, Hsiao H, Teng C, Lee H (2025) Constructing deep learning datasets
810 to reveal climate trends of tropical cyclone intensity and structure extremes. Artif
811 Intell Earth Syst 4:e240064. https://doi.org/10.1175/AIES-D-24-0064.1
812 Combot C, Mouche J, Knaff Y, Zhao Y, Zhao L, Vinour Y, Quilfen B (2020) Extensive
813 high-resolution synthetic aperture radar (SAR) data analysis of tropical cyclones:
814 Comparisons with SFMR flights and best track. Mon Weather Rev 148:4545–4563.
815 https://doi.org/10.1175/MWR-D-20-0005.1
816 DeMaria M, Franklin JL, Chirokova G, Radford J, DeMaria R, Musgrave KD, Ebert-
817 Uphoff I (2025) An operations-based evaluation of tropical cyclone track and
818 intensity forecasts from artificial intelligence weather prediction models. Artif Intell
819 Earth Syst 4:e240085. https://doi.org/10.1175/AIES-D-24-0085.1
820 Dvorak VF (1984) Tropical cyclone intensity analysis using satellite data. NOAA Tech

Rep 11

Emanuel K, Rotunno R (2011) Self-stratification of tropical cyclone outflow. Part I: Implications for storm structure. J Atmos Sci 68:2236–2249. https://doi.org/10.1175/JAS-D-10-05024.1

Hersbach H, et al (2020) The ERA5 global reanalysis. Q J R Meteorol Soc 144:1999–2049. https://doi.org/10.1002/qj.3803

Hersbach H, Bell B, Berrisford P, Biavati G, Horányi A, Muñoz Sabater J, Nicolas J, Peubey C, Radu R, Rozum I, Schepers D, Simmons A, Soci C, Dee D, Thépaut J-N (2023) ERA5 monthly averaged data on pressure levels from 1940 to present. https://doi.org/10.24381/cds.6860a573. Copernicus Climate Change Service (C3S) Climate Data Store (CDS)

Hirano S, Ito K, Yamada H, Tsujino S, Tsuboki K, Wu C-C (2022) Deep eye clouds in Tropical Cyclone Trami (2018) during T-PARCII dropsonde observations. J Atmos Sci 79:683–703. https://doi.org/10.1175/JAS-D-21-0129.1

Howell B, Kucas M, Cowan L, Strahl B, Howard A, Sampson CR (2025) The Joint Typhoon Warning Center tropical cyclone best tracks, 1945–2025. NRL Formal Rep NRL/7550/FR--2025/3. https://www.metoc.navy.mil/jtwc/products/best-tracks/JTWC_TC_Best_Tracks_NRL_Report.pdf. Accessed 4 Mar 2026

839 Ito K, Miyamoto Y, Wu C-C, Didlake A, Hlywiak J, Huang Y-H, Lai T-K, Pattie L, Qin
840 N, Shimada U, Tao D, Yamada Y, Zhang J, Kanada S, Herndon D (2025) Recent
841 research and operational tools for improved understanding and diagnosis of tropical
842 cyclone inner core structure. J Meteorol Soc Japan 103:147–180.
843 https://doi.org/10.2151/jmsj.2025-008
844 Jorgensen DP (1984) Mesoscale and convective-scale characteristics of mature hurricanes.
845 Part II: Inner-core structure of Hurricane Allen (1980). J Atmos Sci 41:1287–1311.
846 https://doi.org/10.1175/1520-0469(1984)041<1287:MACSCO>2.0.CO;2
847 Knaff JA, Longmore SP, DeMaria RT, Molenar DA (2015) Improved tropical-cyclone
848 flight-level wind estimates using routine infrared satellite reconnaissance. J Appl
849 Meteorol Climatol 54:463–478. https://doi.org/10.1175/JAMC-D-14-0112.1
850 Kubota T, et al (2007) Global precipitation map using satelliteborne microwave
851 radiometers by the GSMaP project: Production and validation. IEEE Trans Geosci
852 Remote Sens 45:2259–2275. https://doi.org/10.1109/TGRS.2007.895337
853 Kubota T, Shige S, Aonashi K, Okamoto K (2009) Development of nonuniform
854 beamfilling correction method in rainfall retrievals for passive microwave
855 radiometers over ocean using TRMM observations. J Meteorol Soc Japan 87A:153–
856 164. https://doi.org/10.2151/jmsj.87A.153

857 Kossin JP, Knaff JA, Berger HI, Herndon DC, Cram TA, Velden CS, Murnane RJ,
858 Hawkins JD (2007) Estimating hurricane wind structure in the absence of aircraft
859 reconnaissance. Weather Forecast 22:89–101. https://doi.org/10.1175/WAF985.1
860 Lajoie F, Walsh K (2008) A technique to determine the radius of maximum wind of a
861 tropical cyclone. Weather Forecast 23:1007–1015.
862 https://doi.org/10.1175/2008WAF2007077.1
863 Li Y, Wang Y, Tan Z-M (2022) How frequently does rapid intensification occur after rapid
864 contraction of the radius of maximum wind in tropical cyclones over the North
865 Atlantic and eastern North Pacific? Mon Weather Rev 150:1747–1760.
866 https://doi.org/10.1175/MWR-D-21-0322.1
867 Liu G, Jiang S, Zheng M (2025) A global ERA5-based tropical cyclone wind field dataset
868 enhanced by integrated parametric correction methods. Sci Data 12:1429.
869 https://doi.org/10.1038/s41597-025-05789-w
870 Lu X, Wong W, Yu H, Yang X (2022) Tropical cyclone size identification over the western
871 North Pacific using support vector machine and general regression neural network.
872 J Meteorol Soc Japan 100:927–941. https://doi.org/10.2151/jmsj.2022-048
873 Mallen KJ, Montgomery MT, Wang B (2005) Reexamining the near-core radial structure
874 of the tropical cyclone primary circulation: Implications for vortex resiliency. J

875 Atmos Sci 62:408–425. https://doi.org/10.1175/JAS-3377.1
876 Mouche A, Chapron B, Zhang B, Husson R (2017) Combined co- and cross-polarized
877 SAR measurements under extreme wind conditions. IEEE Trans Geosci Remote
878 Sens 55:6746–6755. https://doi.org/10.1109/TGRS.2017.2732508
879 Mouche A, Chapron B, Knaff JA, Zhao Y, Zhang B, Combot C (2019) Copolarized and
880 cross-polarized SAR measurements for high-resolution description of major
881 hurricane wind structures: Application to Irma Category 5 hurricane. J Geophys Res
882 Oceans 124:3905–3922. https://doi.org/10.1029/2019JC015056
883 Mouche A, Avenas A, et al (2026) Fostering tropical cyclone research and applications
884 with synthetic aperture radar. Remote Sens Environ 333:115139.
885 https://doi.org/10.1016/j.rse.2025.115139
886 Mueller KJ, DeMaria M, Knaff JA, Kossin JP, Vonder Haar TH (2006) Objective
887 estimation of tropical cyclone wind structure from infrared satellite data. Weather
888 Forecast 21:990–1005. https://doi.org/10.1175/WAF955.1
889 NASA (2026) Earthdata search. https://search.earthdata.nasa.gov. Accessed 4 Mar 2026
890 Nishimura S, Sasaki M, Nonaka N, Ueno M, Mochizuki Y, Miura M (2023) The Japan
891 Meteorological Agency's Dvorak re-analysis data. RSMC Tokyo – Typhoon Center
892 Tech Rev. https://www.jma.go.jp/jma/jma-eng/jma-center/rsmc-hp-pub-

893 eg/techrev/text26-1.pdf. Accessed 4 Mar 2026
894 Razin MN, Slocum CJ, Knaff JA, Brown PJ (2023a) Tropical cyclone precipitation,
895 infrared, microwave, and environmental dataset (TC PRIMED).
896 https://doi.org/10.25921/dmy1-0595
897 Razin MN, Slocum CJ, Knaff JA, Brown PJ, Bell MM (2023b) Tropical cyclone
898 precipitation, infrared, microwave, and environmental dataset (TC PRIMED). Bull
899 Am Meteorol Soc 104:E1980–E1998. https://doi.org/10.1175/BAMS-D-21-0052.1
900 Rogers R (2023) The World Meteorological Organization Tenth International Workshop
901 on Tropical Cyclones (IWTC-10): A summary. Trop Cyclone Res Rev 12:1–9.
902 https://doi.org/10.1016/j.tcrr.2023.04.001
903 Shimada U (2025) Estimation of the radius of maximum wind using passive microwave
904 satellite data. SOLA 21:265–272. https://doi.org/10.2151/sola.2025-033
905 Shimada U, Tsukada T (2026) Data for “A Long-Term Tropical Cyclone RMW Dataset
906 in the Western North Pacific Based on a Bayesian Consensus of Multiple Estimates”.
907 https://doi.org/10. 10.5281/zenodo.20406310 Accessed 27 May 2026
908 Shimada U, Aonashi K, Miyamoto Y (2017) Tropical cyclone intensity change and
909 axisymmetricity deduced from GSMaP. Mon Weather Rev 145:1003–1017.
910 https://doi.org/10.1175/MWR-D-16-0244.1

911 Shimada U, Owada H, Yamaguchi M, Iriguchi T, Sawada M, Aonashi K, DeMaria M,
912 Musgrave KD (2018) Further improvements to the statistical hurricane intensity
913 prediction scheme using tropical cyclone rainfall and structural features. Weather
914 Forecast 33:1587–1603. https://doi.org/10.1175/WAF-D-18-0021.1
915 Shimada U, Hayashi M, Mouche A (2024) A comparison between SAR wind speeds and
916 western North Pacific tropical cyclone best track estimates. J Meteorol Soc Japan
917 102:575–593. https://doi.org/10.2151/jmsj.2024-031
918 Sitkowski M, Kossin JP, Rozoff CM (2011) Intensity and structure changes during
919 hurricane eyewall replacement cycles. Mon Weather Rev 139:3829–3847.
920 https://doi.org/10.1175/MWR-D-11-00034.1
921 STAR (2026) Tropical cyclone winds.
922 https://www.star.nesdis.noaa.gov/socd/mecb/sar/sarwinds_tropical.php. Accessed 4
923 Mar 2026
924 Stern DP, Vigh JL, Nolan DS, Zhang F (2015) Revisiting the relationship between eyewall
925 contraction and intensification. J Atmos Sci 72:1283–1306.
926 https://doi.org/10.1175/JAS-D-14-0261.1
927 Tao, D., Nystrom, R.G., Chavas, D.R., Avenas, A. (2026) A fast analytical model for the
928 complete radial structure of tropical cyclone low-level wind field. Geophys Res Lett

929 53, e2025GL118320. https://doi.org/10.1029/2025GL118320
930 Tsukada T, Horinouchi T (2023) Strong relationship between eye radius and radius of
931 maximum wind of tropical cyclones. Mon Weather Rev 151:569–588.
932 https://doi.org/10.1175/MWR-D-22-0106.1
933 Tsukada T, Knaff J, Shimada U, Mouche A, Miller S (2025) Guidance for estimating mean
934 winds in tropical cyclone using SAR derived winds. Weather Forecast 40:2699–2716.
935 https://doi.org/10.1175/WAF-D-25-0059.1
936 Vickery PJ, Wadhera D (2008) Statistical models of Holland pressure profile parameter
937 and radius to maximum winds of hurricanes from flight-level pressure and H*Wind
938 data. J Appl Meteorol Climatol 47:2497–2517.
939 https://doi.org/10.1175/2008JAMC1837.1
940 Vinour L, Jullien S, Mouche A, Combot C, Mangeas M (2021) Observations of tropical
941 cyclone inner-core fine-scale structure, and its link to intensity variations. J Atmos
942 Sci 78:3651–3671. https://doi.org/10.1175/JAS-D-20-0245.1
943 Willoughby HE, Rahn ME (2004) Parametric representation of the primary hurricane
944 vortex. Part I: Observations and evaluation of the Holland (1980) model. Mon
945 Weather Rev 132:3033–3048. https://doi.org/10.1175/MWR2831.1
946 Willoughby HE, Clos JA, Shoreibah MB (1982) Concentric eye walls, secondary wind

maxima, and the evolution of the hurricane vortex. J Atmos Sci 39:395–411. https://doi.org/10.1175/1520-0469(1982)039<0395:CEWSWM>2.0.CO;2

Wu Q, Ruan Z (2021) Rapid contraction of the radius of maximum tangential wind and rapid intensification of a tropical cyclone. J Geophys Res Atmos 126:e2020JD033681. https://doi.org/10.1029/2020JD033681

Yamaguchi M, Ikuta Y, Ito K, Satoh M (2025) Tropical cyclone track and intensity predictions in the western North Pacific basin using Pangu-Weather and JMA initial conditions. J Meteorol Soc Japan 103:357–370. https://doi.org/10.2151/jmsj.2025-018

Zhuo JY, Tan ZM (2021) Physics-augmented deep learning to improve tropical cyclone intensity and size estimation from satellite imagery. Mon Weather Rev 149:2097–2113. https://doi.org/10.1175/MWR-D-20-0333.1

Zhuo JY, Tan ZM (2023) A deep-learning reconstruction of tropical cyclone size metrics 1981–2017: Examining trends. J Clim 36:5103–5123. https://doi.org/10.1175/JCLI-D-22-0714.1

Figure Legends

Fig. 1 (a) Scatter plot of R_{mp} (km) versus SAR-derived RMW (km). Black circles denote samples used in the regression (red line), and white circles denote excluded samples. (b) Distribution of $RMW_{\mathrm{GSMaP}}^{\mathrm{TS+}}$ errors (km), with Gaussian fits for all samples (gray) and for samples excluding outliers determined by a threshold value of 28.8 km (red). Sample size (N), median absolute deviation (MAD), criterion for outlier exclusion ($\pm 1.645\hat{\sigma}_{\mathrm{MAD}}$), mean absolute error (MAE), and correlation coefficient (Corr) are shown. MAE and Corr are calculated using all samples, including outliers.

Fig. 2 (a) Scatter plot of $RMW_{\mathrm{GSMaP}}^{\mathrm{TD}}$ (km) versus ASCAT-derived RMW (km). The blue shading indicates kernel density estimation ($\times 10^{-5}$ km^{-2}). (b) Distribution of $RMW_{\mathrm{GSMaP}}^{\mathrm{TD}}$ errors (km), with Gaussian fits for all samples (gray) and for samples excluding outliers determined by a threshold value of 202.5 km (red). Sample size (N), median absolute deviation (MAD), criterion for outlier exclusion ($\pm 1.645\hat{\sigma}_{\mathrm{MAD}}$), mean absolute error (MAE), and correlation coefficient (Corr) are shown. MAE and Corr are calculated using all samples, including outliers.

Fig. 3 (a) Scatter plot of JMA V_{max} (m s^{-1}) versus SAR-based V_{max} (m s^{-1}) derived from

the azimuthally averaged wind speed. The dashed line denotes the 1:1 line. (b) Two-dimensional histogram of V_{ERA5} and SAR wind speeds sampled outside R_{mERA5}. The black line indicates the regression given by Eq. (3). (c) Example of radial profiles of the azimuthally averaged SAR wind speed (red), V_{ERA5} (green), V'_{ERA5} (blue), and the modified Rankine vortex (black) constructed using α determined from R_{12}, R_{mERA5}, and V_{mERA5}. (d) Scatter plot of $RMW^{\mathrm{TS+}}_{\mathrm{Rankine}}$ (km) versus SAR-derived RMW (km). (e) Scatter plot of the mean of $RMW^{\mathrm{TS+}}_{\mathrm{Rankine}}$ and $RMW^{\mathrm{TS+}}_{\mathrm{GSMaP}}$ (km) versus SAR-derived RMW (km). (f) Distribution of $RMW^{\mathrm{TS}}_{\mathrm{Rankine}}$ errors (km), with Gaussian and log-normal fits. Gaussian fits are derived from all samples (gray) and from samples excluding outliers determined by a threshold value of 31.3 km (red). The log-normal fit (blue) is derived from samples with $\varepsilon < 14.0$ km ($N = 106$). Sample size (N), median absolute deviation (MAD), criterion for outlier exclusion ($\pm 1.645\hat{\sigma}_{\mathrm{MAD}}$), mean absolute error (MAE), and correlation coefficient (Corr) are shown. MAE and Corr are calculated using all samples, including outliers. In (a–b), the samples are taken from the period 2015–2023, whereas the samples in (d–f) are taken from the period 2015–2024.

Fig. 4 (a) Scatter plot of $RMW^{\mathrm{TD}}_{\mathrm{ERA5}}$ (km) versus the ASCAT-derived RMW (km). The

999 blue shading indicates kernel density estimation ($\times 10^{-5}$ km^{-2}). (b) Distribution of
1000 $RMW_{\mathrm{ERA5}}^{\mathrm{TD}}$ errors (km), with Gaussian fits for all samples (gray) and for samples
1001 excluding outliers determined by a threshold value of 180.8 km (red). Sample size
1002 (N), median absolute deviation (MAD), criterion for outlier exclusion
1003 ($\pm 1.645\hat{\sigma}_{\mathrm{MAD}}$), mean absolute error (MAE), and correlation coefficient (Corr) are
1004 shown. MAE and Corr are calculated using all samples, including outliers.
1005
1006 **Fig. 5** (a) As in Fig. 3f, but for RMW_{IR} (km). The log-normal fit (blue) is derived from
1007 samples with ε < 9.0 km (N = 67). (b) As in Fig. 3f, but for RMW_{PMW} (km). The
1008 log-normal fit (blue) is derived from samples with ε < 7.0 km (N = 123).
1009
1010 **Fig. 6** (top) Posterior probability distributions obtained with and without an outlier
1011 distribution. (bottom) Individual error distributions corresponding to the RMW
1012 estimates.
1013
1014 **Fig. 7** Hovmöller diagrams of (a) linearly normalized precipitation, (b) relocated
1015 precipitation, and (c) the error distribution term of the $RMW_{\mathrm{GSMaP}}^{\mathrm{TS+}}$ likelihood for
1016 Typhoon Mawar (2023).

Fig. 8 Hovmöller diagrams of the posterior probability distribution of the RMW (a) before and (b) after smoothing for Typhoon Mawar (2023).

Fig. 9 Relationships between (a) JMA V_{max} (m s^{-1}) and bias (consensus minus SAR-derived RMW; km) and (b) posterior probability and bias (km). Black circles denote dependent samples, and red circles denote independent samples.

Fig. 10 (a) Scatter plot of SAR-derived RMW (km) versus consensus RMW (km). The dashed line denotes the 1:1 line. Sample size (N), mean absolute error (MAE), root-mean-square error (RMSE), bias, correlation coefficient (Corr), and coefficient of determination R^2 are shown. (b–c) Boxplots of absolute errors stratified by JMA V_{max} (m s^{-1}) and posterior probability, respectively. A cross denotes the MAE for each group, and circles denote outliers. Sample size (N) and bias are shown.

Fig. 11 Temporal evolution of the consensus RMW estimates (thick black line) together with the individual estimates for Typhoon Mawar (2023). White circles denote SAR-derived RMWs as reference.

Fig. 12 (a) As in Fig. 11, but for Tropical Storm Barijat (2024). Vertical lines indicate the times shown in (c) and (d). The V_{max} of 18 m s^{-1} at 0600 UTC 5 October results from extrapolation during the TD stage (see Sect. 2). (b) Hovmöller diagram of the posterior probability distribution of the RMW. The thick black line denotes the radius of maximum posterior probability. (c–d) ASCAT wind fields at ~2330 UTC 4 October and ~2310 UTC 7 October, respectively, with the corresponding visible imagery overlaid. The yellow circles indicate a radius of 50 km in (c), and radii of 100 km and 300 km in (d). In (d), the TC center in the ASCAT wind field appears displaced from that in the visible imagery, possibly due to the coarse spatial resolution of ASCAT (25 km).

Fig. 13 Two-dimensional histograms of 6-hourly (a) JTWC V_{max} (m s^{-1}) versus consensus RMW (km) and (b) JTWC V_{max} (m s^{-1}) versus JTWC best track RMW (km) during 2001–2025. White circles denote SAR-derived RMWs and their corresponding JTWC V_{max} values during 2015–2025. Black and red boxes indicate areas I and II, respectively.

Fig. 14 Boxplots of (a) bias and (b) absolute error of JTWC and consensus RMWs against SAR-derived RMWs, stratified by Saffir-Simpson hurricane wind scale categories based on JTWC V_{max}. A cross denotes the MAE for each group, and circles denote outliers. Sample size (N) is shown below the category name. The numbers indicated in teal represent out-of-range outliers beyond ± 100 km.

Tables

Table 1: Error distribution parameters of the RMW estimation methods used in the consensus framework.

Estimates	Applicable case	Error distribution	μ [km]	σ [km]	U [km]
$RMW_{\mathrm{GSMaP}}^{\mathrm{TS+}}$	$V_{\max} \geq 18$ m s^{-1}	Normal	1.359	10.617	–
$RMW_{\mathrm{GSMaP}}^{\mathrm{TD}}$	$V_{\max} < 20$ m s^{-1}	Normal	–5.977	81.914	–
$RMW_{\mathrm{Rankine}}^{\mathrm{TS+}}$	$V_{\max} \geq 18$ m s^{-1}	Log-normal	2.981	0.776	14
$RMW_{\mathrm{ERA5}}^{\mathrm{TD}}$	$V_{\max} < 20$ m s^{-1}	Normal	–3.846	67.849	–
RMW_{IR}	Dvorak eye pattern	Log-normal	2.066	0.599	9
RMW_{PMW}	$V_{\max} > 33$ m s^{-1}	Log-normal	2.045	0.518	7